The Dissertation for Doctoral Degree

STUDY ON PLASMA EMISSION BEHAVIOR DURING PLASMA ELECTROLYTIC OXIDATION (PEO) ON MAGNESIUM ALLOY

The dissertation submitted to

Tokushima University

in partial fulfillment of the requirements

for the doctoral degree

by

GIRASE KRUNAL GAJENDRASING

Under guidance of

PROF. YOSHIHIRO DEGUCHI

Mechanical engineering

Intelligent structures and mechanics system engineering

Graduate School of Advanced Technology and Science

Tokushima University, Japan

September 2020

ACKNOWLEDGMENT

Table of Content

List of Figures

List of Table

List of symbols and abbreviations

PEO	Plasma Electrolytic Oxidation
ICCD	Intensified Charged Coupled Device
OES	Optical Emission Spectroscopy
MAO	Micro-arc oxidation
MPO	Micro-plasma oxidation
ASD	Anodic spark deposition
SEM	Scanning electron microscope
SUS	Stainless steel
Mg	Magnesium
Na-I	Sodium atom
SiC	Silicon carbide
Al	Aluminum
Zn	Zinc
Mn	Manganese
Si	Silicon
Cu	Copper
Fe	Iron
cm	Centimeter (unit of length)
cm^2	Square centimeter (unit of length)
mm^2	Square millimeter (unit of length)
mm	Millimeter (unit of length)
nm	Nano-meter (unit of length)
V	Voltage
mV	Milli-volt
mA	Milli-ampere (Unit of electrical current)
A	Ampere (Unit of electrical current)
µs	Micro-second (unit of time)
s	Second (unit of time)
ms	Millisecond (unit of time)
T	Temperature
K	Kelvin (unit of temperature)

H	Hydrogen
NUV	Near-ultraviolet
%	Percentage
Hz	Hertz (unit of frequency)
kHz	Kilo-Hertz (unit of frequency)
MHz	Mega-Hertz (unit of frequency)
W	Watt (unit of power)
L	Liter (Unit of volume)
pH	Potential for hydrogen

ABSTRACT

The high sensitivity of magnesium weakens the corrosion and wear resistance of this metal and its alloys, especially in corrosion media. The protection of magnesium and its alloys from corrosion is a significant concern in a real application. A great effort has been made in the last few decades to solve this problem. The proper surface treatment can improve corrosion and wear resistance of magnesium and its alloys. Various types of surface coatings have been developed to provide corrosion protection, among which plasma electrolytic oxidation (PEO) is one of the most promising techniques. The PEO treatment can produce a hard ceramic-like oxide coating on magnesium and its alloys, leading to significantly enhanced wear and corrosion resistance. However, the intrinsic porous morphology of the PEO coatings still limits their effect of corrosion protection. The plasma during the PEO coating formation responsible for these microstructural drawbacks. Controlling the plasma during the process can improve the formed coating quality.

The objective of this study is to overcome these microstructural drawbacks and further improve the quality of PEO coatings. Therefore, the time-dependent plasma behavior was studied in terms of emission intensity and plasma temperature. The bipolar current pulse mode was applied to the sample to form a zirconia oxide coating on AZ91D Mg-alloy by the PEO process. The plasma emission and output anodic voltage were investigated by changing the ON / OFF timing of bipolar pulse current cycle and the ratio of anodic to cathodic current at the same frequency and duty ratio. The spatial and time resolved measurement approach was adopted to study the time dependent plasma emission behavior during the PEO process. The plasma emission during the PEO process was monitored using Intensified Charged Coupled Device (ICCD) camera concerning time. The measured spatially resolved and time resolved emission during anodic pulse was characterized using Optical Emission Spectroscopy (OES) and further plasma temperature throughout the PEO process. The time averaged and time resolved with spatially resolved plasma emission was also monitored using photodetector during anodic pulse throughout the PEO process. The plasma images were also used to study plasma emission behavior during the PEO process.

It was found that changes in the ON / OFF timing of bipolar pulse current effect on plasma stability and variation in output anodic voltage. Change in the current ratio (anodic to cathodic) at the same frequency and duty ratio effect on the appearance of plasma spark during the PEO

process. The current ratio of greater than 1 shows the continuous increase and then stabilization in emission intensity with a gradual increase in voltage throughout the PEO process. In contrast, the current ratio of less than 1, a sudden drop in plasma emission intensity with voltage, was found during the process. Therefore, the PEO process can be divided into two regimes, 'arc regime' and 'soft regime' before and after voltage drop, respectively. Results of measured emission spectra using ICCD camera shows that arc regime has atomic or ionic excitation. However, the soft regime does not have atomic or ionic excitation during the PEO process. The plasma temperature in the arc regime was found varying in the range of 4200 K to 6400 K, which was calculated using the relative emission intensity of Na-I optical lines. However, the plasma temperature in the soft regime could not be calculated because of no atomic or ionic excitation during the process. The emission due to collision radiative recombination in arc regime was found after 130 µs of anodic pulse time in emission spectra during the PEO process. The emission intensity and the plasma temperature show stable behavior until 130 µs of anodic pulse time and 1800 s of the PEO process time and increase with time. Therefore, it can be said that high-intensity plasma discharges, which are responsible for microstructural drawbacks in the formed coating, observed after anodic pulse 130 µs and processing time of 1800 s. It is demonstrated that the growth of the porous layer during the PEO process can be controlled by controlling these timings, which is benefit for the protective oxide coating on the sample. Therefore, the PEO process can be controlled by regulating; the anodic to cathodic current ratio, the ON / OFF timing of bipolar current pulse, and the PEO process time to improve the performance of the alloy.

KEYWORDS: Plasma Electrolytic Oxidation (PEO); Spatial resolved and time-resolved plasma emission; Bipolar pulse timing; Anodic to Cathodic current ratio; Intensified Charge-Coupled Device (ICCD) camera; Photodetector

Chapter 1

Introduction

1.1 Background

Owing to the advantages, such as low density and high strength-to-weight ratio, good electric shielding effect and excellent damping capacity, good thermophysical properties, biocompatibility and recyclability potential, magnesium and its alloys have long been regarded as materials of choice for many industrial applications [1-11]. The usage of magnesium, as the lightest structural metal on earth, has significantly increased during the last decade because of the increasing importance of weight saving in many products, especially related to aerospace, transportation, and electronics [10]. However, the high susceptibility to corrosion has significantly restricted further applications of magnesium alloys, and effective methods are currently being sought to deal with this issue. To date, a great deal of research focusing on understanding the corrosion behavior and enhancement of corrosion protection of magnesium alloys has been carried out [11-27]. Among these studies, plasma electrolytic oxidation (PEO) coatings have attracted significant attention since they can provide relatively good protection for lightweight valve metals, such as aluminum, magnesium, titanium, and zirconium [23-24, 28-33].

As one of the promising techniques, plasma electrolytic oxidation (PEO) is a plasma-assisted electrochemical surface treatment which develops from the conventional anodizing process, but with a much higher voltage/current applied on the samples. Generally, PEO treatments are processed with both anode (samples), and a cathode (noble materials such as SUS) immersed in an environmentally-friendly alkaline electrolyte bath. During the PEO treatment, sparks caused by discharging events can be observed on the surface of the sample. PEO coatings can significantly improve the corrosion resistance of magnesium alloys by forming hard oxide coatings on the metal substrate. However, the porous morphology and relatively loose structure compared with PEO coatings on aluminum still limit the corrosion protection ability of the PEO coatings on magnesium. To overcome these drawbacks, great efforts have been made to optimize the electrical parameters and/or modify the electrolyte composition, which is aimed at producing high quality PEO coatings on magnesium by improving the coating microstructure.

1.2 Aim and Objective

In this study, zirconium oxide coating was formed using the PEO process on AZ91D Mg-alloy, aiming to overcome the intrinsic drawbacks of the PEO coatings like microcracks and porosity, and further improve the coating quality. In particular, the influence of electrical parameters on the PEO coating and plasma emission behavior was firstly investigated. Then, a spatial and time resolved measurement approach was used to study plasma emission behavior using Intensified Charged Coupled Device (ICCD) camera. The measured spatially resolved and time resolved emission during anodic pulse was characterized using Optical Emission Spectroscopy (OES) and further plasma temperature throughout the PEO process. The time averaged and time resolved with spatially resolved plasma emission was also monitored using photodetector during anodic pulse throughout the PEO process. Considering the overall aim, as well as the methods, the following specific objectives need to be identified:

(1) Study the influence of bipolar pulse timing on the plasma emission behavior during the PEO process on Mg-alloy.

(2) Study the influence of anodic to cathodic current ratio on the plasma emission behavior during the PEO process on Mg-alloy.

(3) Study the plasma emission behavior using a spatial and time resolved measurement approach to evaluate the optimum PEO working conditions to achieve impermeable ZrO_2 coating on Mg-alloy.

(4) Reveal the plasma formation model with time during the PEO process on Mg-alloy.

1.3 Thesis Overview

Chapter 2 introduces the general principles and characteristics of PEO processes with the formation mechanism of the PEO coating, as well as the morphology, microstructure, and phase composition of the PEO coatings on magnesium and its alloys. This chapter also discusses recent developments relating to PEO coatings on magnesium and its alloys.

Chapter 3 briefly introduce the experimental methods and optical arrangements used in this work using measurement devices as the ICCD camera and a photodetector. The application of these measurement methods enables a comprehensive understanding of the plasma emission behavior during the PEO process. It also provides an effective means to fulfill the objectives mentioned above.

Chapter 4 briefly introduce the effect of electrical parameters on output anodic voltage and plasma stability. This chapter also discusses the reason for choosing the input electrical parameters and bipolar pulse time to study spatially resolved and time resolved plasma emission behavior. The evaluation of special and time resolution is also explained in this chapter.

Chapter 5 introduce the plasma emission behavior concerning an anodic pulse time and the PEO processing time. The emission results using special and time resolved measurement approach by the ICCD camera and a photodetector is discussed in this chapter. The evaluation of processing parameters to control the PEO process is also explained in this chapter.

Chapter 6 introduce the anodic output voltage concerning the PEO processing time with plasma discharging appearance. Depending on the anodic voltage behavior, discharge appearance is explained in four stages. The plasma discharge model is also interpreted based on the emission results.

Chapter 7 introduce the effect of applied current density on plasma emission behavior with time during the PEO process. The introduction of the soft regime by controlling the anodic to cathodic current ratio is discussed in this chapter.

Chapter 8 summarizes all of the findings and concludes the results during this research study.

Chapter 2

Introduction to Plasma Electrolytic Oxidation on Magnesium and its alloys

2.1 General principle and characteristics of the PEO process

Plasma Electrolytic Oxidation (PEO), which is also known as micro-arc oxidation (MAO) [34], micro-plasma oxidation (MPO) [28], and anodic spark deposition (ASD) [35], is a plasma-assisted electrochemical surface treatment of lightweight valve metals such as magnesium, aluminum, and titanium. Due to the excellent properties, PEO coatings have been widely applied in various fields like automotive, sports, aerospace, oil, and gas industries. As a relatively novel and promising surface coating technique, PEO has recently attracted extensive attention from both academics and industrialists across the world [3,30-32, 35-44]. In this section, the fundamental principles and characteristics of the PEO process, as well as recent developments in PEO coatings on Mg and its alloys are discussed.

2.1.1 Characteristics of the PEO process

The PEO process is usually carried out in a neutral or alkaline electrolyte, with both working electrode (metal substrate) and counter electrode (typically stainless steel) serving as the anode and cathode, respectively. The energy required for the PEO treatment is provided by an external power supply which connects the electrodes immersed in the electrolyte. The whole system is similar to that used in conventional anodizing treatment, with an only significant difference in the applied voltage.

The electrode processes during the PEO treatment are schematically illustrated in Figure 2-1. Gas liberation is a typical phenomenon in the PEO treatment, which can be observed on the surface of both anode and cathode. To be specific, gaseous oxygen and hydrogen are generated and released at the surface of the anode and cathode, respectively. Accompanied by the gas liberation, metal oxidation on the anodic surface and cation reduction on the cathodic surface also occur simultaneously. During the PEO treatment, the operating voltage applied to the electrodes exceeds the dielectric breakdown potential of the oxide film, resulting in a large number of micro-discharges occurring on the surface of the metal substrate. These discharges are a very critical factor for the coating formation process, which helps the incorporation of

electrolyte compounds into the coating matrix and sintering the oxide film. With the assistance of discharges, a ceramic coating can be formed following electrochemical reactions at the metal-electrolyte interface. Therefore, the properties of PEO coatings, such as hardness, wear, and corrosion resistance, are usually better compared with conventional anodizing films.
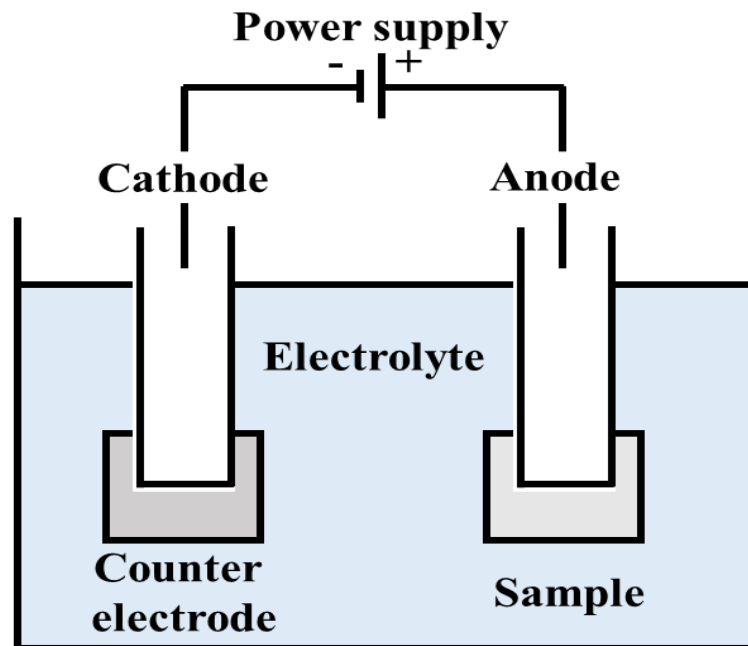
Figure 2-1 Typical Plasma electrolytic oxidation setup.

Moreover, acoustic and optical emissions, as well as heating effects due to the discharging activity, also can be observed in the PEO process, which would continuously consume energy. It has to be noted that the oxidation process that occurred on the anode can not only lead to the formation of the oxide film but also cause metal dissolution, which depends on the electrolyte composition. Besides, gas liberation in the PEO treatment is stronger than conventional anodizing, which can significantly influence the results under certain conditions, indicating the complexity of PEO processes.

2.1.2. The formation mechanism of the PEO coating on Mg and its alloys

Generally, the formation mechanism study of the coating may help to understand the procedure and to evaluate optimum conditions to achieve good quality. Recently, the PEO coating formation mechanism has attracted significant attention [45-49]. The formation mechanism of the PEO coating is somehow complicated due to many electrochemical, chemical, and thermal reactions [50–54]. Oxide film formation, primary film dissolution, and evolution of gas on

anode surface constitute the main reaction in a PEO process. The dominance of any of these reactions depends on magnesium alloy composition, electrolyte type, the concentration of each component in the electrolyte, and applied current density. Figure 2-2 [55] shows a systematic characterization of all comprehensive methods to study PEO coatings on magnesium and its alloys.
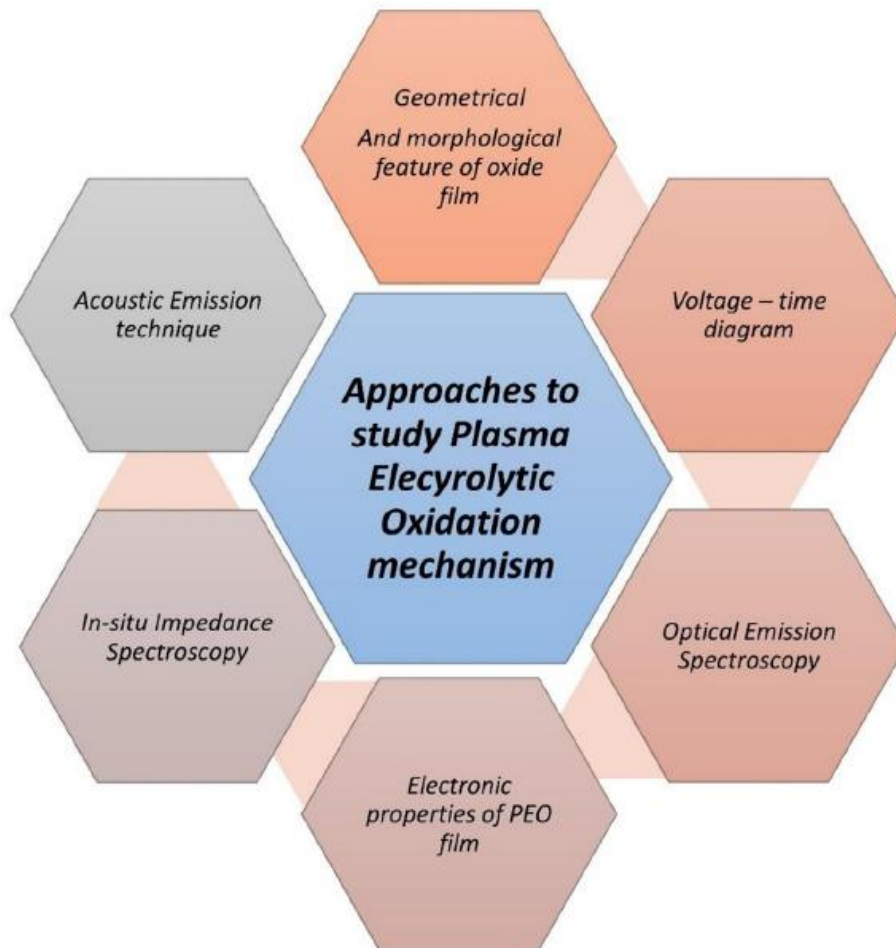
Figure 2-2 Schematic of different approaches to studying the plasma electrolytic oxidation mechanism. [55]

Despite the applied metal substrate and electrical regime, the basic principles, and mechanisms of the PEO process are similar for treatments of various metals. Based on the voltage/current transients, the coating formation kinetics are usually described as three or four different stages, depending on the interpretation of the PEO process [56-62]. Although disagreement exists in dividing coating evolution during the PEO process, there is no essential difference among these theories.

For example, the PEO treatment of Mg in alkaline electrolytes can be categorized into three stages. Ko et al. [56] presented the typical voltage vs. time curves, as shown in Figure 2-3 for the PEO treatment of AZ91 Mg alloy in an alkaline silicate-based electrolyte, showing the three different stages and corresponding characteristics. The first stage is characterized by the passive film formation process, in which $Mg(OH)_2$ and MgO will be formed on the surface of the metal substrate. Concurrently, a dissolution of Mg alloy also takes place in this stage. The substances from the electrolyte can also be detected in the passive film in some cases, indicating the incorporation of electrolyte compounds into the film. Besides, the voltage rapidly increases in this period, with no discharge events observed. The passive film formation process in the first stage can be represented by the following reactions.

$$Mg \rightarrow Mg^{2+} + 2e^-$$
$$Mg^{2+} + 2OH^- \rightarrow Mg(OH)_2$$
$$Mg(OH)_2 \rightarrow MgO + H_2O$$
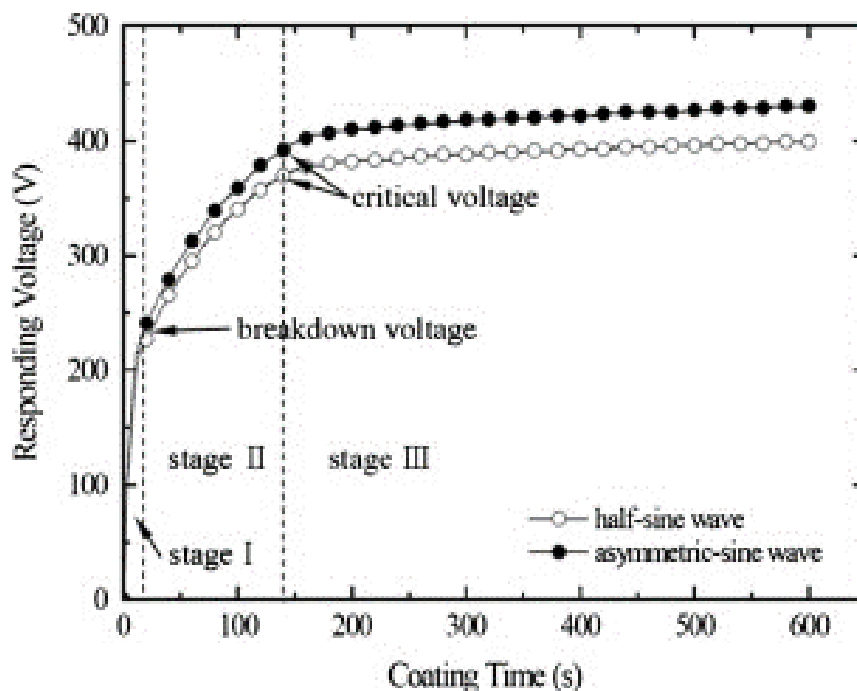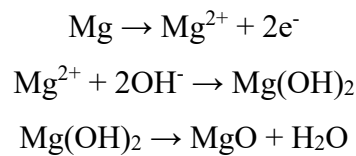
Figure 2-3 Temporal evolution of voltage during the PEO process on AZ91 Mg-alloy. [56]

During the second stage, the voltage still quickly increases with the processing time, but the growth rate becomes slower compared with that in the first stage. One noticeable characteristic that can be observed in this stage is the initiation of discharge phenomena. It can be explained by the increase of applied voltage, which exceeds the breakdown voltage of the passive film.

The discharges observed at this stage are rather fine and bright, with a relatively high density and short life-time.

When the PEO process evolves to the third stage, a prominent characteristic in the voltage vs. time plot is a dramatically decreased voltage growth rate. Due to this, the coating growth rate also becomes slower [63]. Despite the reduced coating growth rate, the voltage applied at this stage reaches a critical value in which the micro-discharges dominate over electrochemical reactions, and the average voltage is much higher than the previous stages. With the increasing processing time, the thickness of oxide film increases, and the average size and intensity of discharges become much more significant and stronger. In contrast, the discharge population decreases significantly compared with that in the previous two stages.

2.2 Microstructure and phase composition of the PEO coatings on Mg

The microstructure of PEO coatings can be influenced by many factors, including electrical parameters, electrolyte composition, and substrate materials. Usually, PEO coatings exhibit a typical porous morphology with numerous micropores and cracks distributed on the coating surface and inside the coating matrix. The micro-pore diameter is generally in the range from less than 1 µm to more than 50 µm, depending on the conditions of the PEO process. Figure 2-4 shows typical SEM surface morphologies of PEO coatings produced on Mg in alkaline electrolytes. It can be seen that pores are uniformly distributed on the surface, with some cracks propagated among them. The porous microstructure is mainly attributed to discharge activity and gas liberation during the PEO treatment [64]. It can also be found that the increased current density caused a coarser surface morphology of PEO coating, which could be explained by the increased energy of discharges. The significant temperature difference across the coating/electrolyte interface causes a relatively high cooling rate of PEO coatings, leading to the initiation of cracks induced by local thermal stress.

Figure 2-5 shows the SEM images illustrating cross-sectional features of PEO coatings produced on Mg at different current densities [65]. The cross-sectional morphology is characterized by the extensive networks of micro-cracks, which is more obvious in thicker coatings (Figure 2-5c). Some cracks even connect the surface of the PEO coating to the metal substrate, as shown by the arrows in Figure 2-5 (b) and (c). It can be seen that PEO coating produced at the lowest current density (Figure 2-5a) has a more compact structure with fewer pores and cracks in the coating matrix compared with thicker coatings produced at higher

current densities. Thus, the high current density can accelerate coating growth but would lead to a coarse microstructure with more pores and cracks. Generally speaking, the factors which can influence the cross-sectional morphology of PEO coating are similar to those affecting the surface morphology, as discussed above.
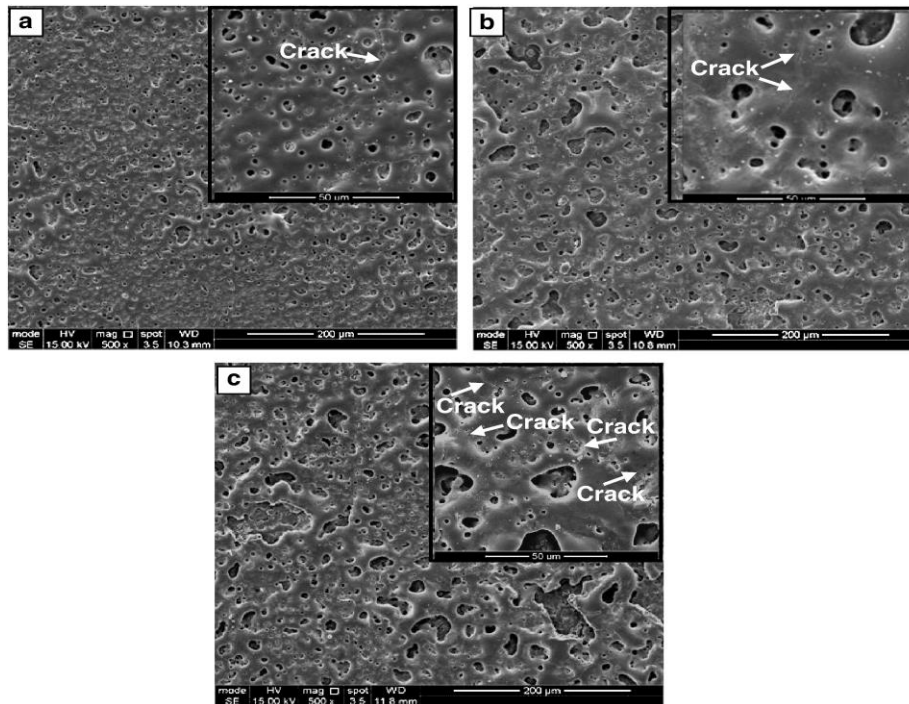
Figure 2-4 SEM images of surface morphology of the PEO coatings produced on Mg in an alkaline electrolyte at current densities (mA/cm^2) of; (a) 30, (b) 40, and (c) 50. [64]

Despite the difference in coating thickness and/or composition, the cross-section of all PEO coatings can be categorized into several regions based on their characteristics. Blawert *et al.* [66] have divided the PEO coating into four distinct regions as illustrated in Figure 2-6: (i) an outer porous region with craters on the surface, (ii) pore bands with obvious pores and discharge channels, (iii) a relatively compact intermediate layer with few pores, (iv) a very dense and thin inner barrier layer. Since the cross-sectional features of PEO coatings produced in various electrolytes and processing conditions can be significantly different, these could also be divided into two or three distinct regions, depending on the working conditions. It has to be noted that features of the microstructure discussed above are typical for all PEO coatings, no matter what substrate and electrolyte are applied in the PEO process.

Porosity is a critical factor that can affect the properties of PEO coatings, especially corrosion resistance. It is directly related to the coating microstructure that can be influenced by the electrical parameters, electrolyte properties, substrate material, and treatment time. These factors play an essential role in discharging activity and gas evolution during the PEO process. In the last decade, extensive studies have been carried out to establish factors influencing the microstructure of PEO coatings [29, 60, 62, 67-70]. Gnedenkov et al. [29] studied the effect of power supply mode on the structure of PEO coatings produced on MA8 Mg alloy in a silicate-containing electrolyte. According to their results, the PEO coating produced in the bipolar mode has low porosity and a more compact microstructure compared that produced in the unipolar mode. Liang et al. [60] reported that the PEO coating produced in the silicate-based electrolyte shows higher microhardness and better corrosion property with relatively dense microstructure and fewer defects (pores and cracks), compared with those formed in the phosphate electrolyte.
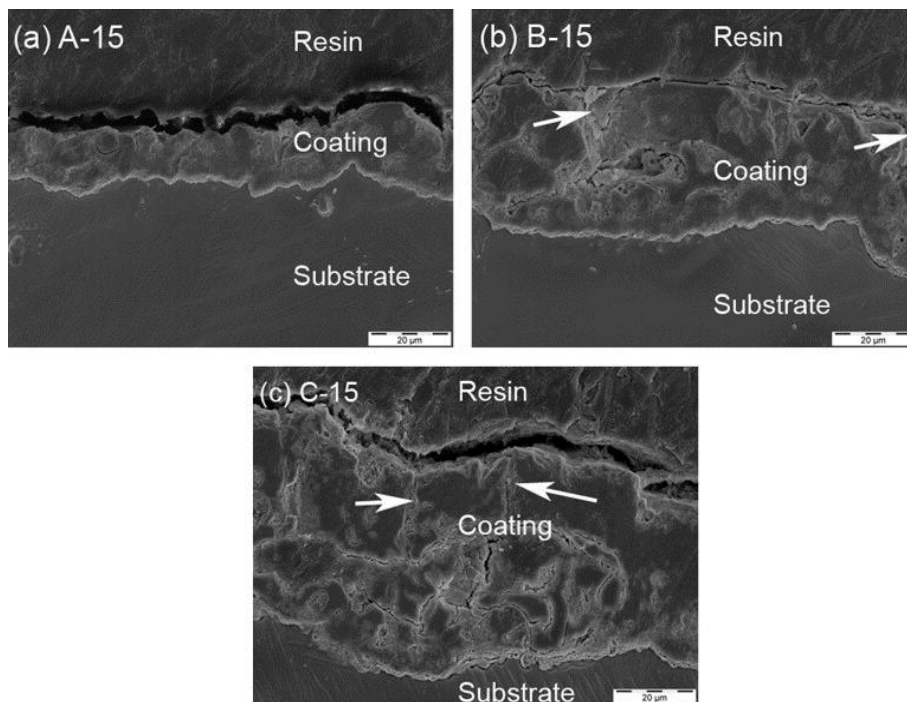
Figure 2-5 SEM images of cross-sectional morphology of the PEO coatings produced on Mg alloy at different current densities (mA/cm^2) of (a) 15, (b) 75, and (c) 150 for 15 min. [65]

The electrolyte composition and substrate material are the two major factors influencing the phase composition of PEO coatings. The majority of published works on PEO coated Mg uses silicate or phosphate-based electrolytes, with some of them containing fluoride or other substances as additives. It is found that MgO, MgAl$_2$O$_4$, MgF$_2$, Mg$_3$(PO$_4$)$_2$, and Mg$_2$SiO$_4$ are

the main phase constituents that can be detected in the PEO coatings on Mg and its alloys [3, 65, 57, 64, 71]. It has to be noted that the phase composition could be different even though the electrolyte composition used in different PEO treatments were similar, indicating the processing parameters also play a role in the phase formation process. Moreover, some additives such as particles can also be incorporated in the PEO coatings.

After analyzing the microstructure and phase composition, the advantages and disadvantages of the PEO coatings on Mg are revealed. As ceramic-like–coatings with relatively good adhesion property and high thickness, PEO coatings could be one of the ideal alternatives of traditional anodizing coatings. However, to meet the stringent requirements for practical applications, additional treatments are usually needed to cover the shortcomings of PEO coatings; for example, post-sealing treatments to deal with microspores and cracks in the coating.
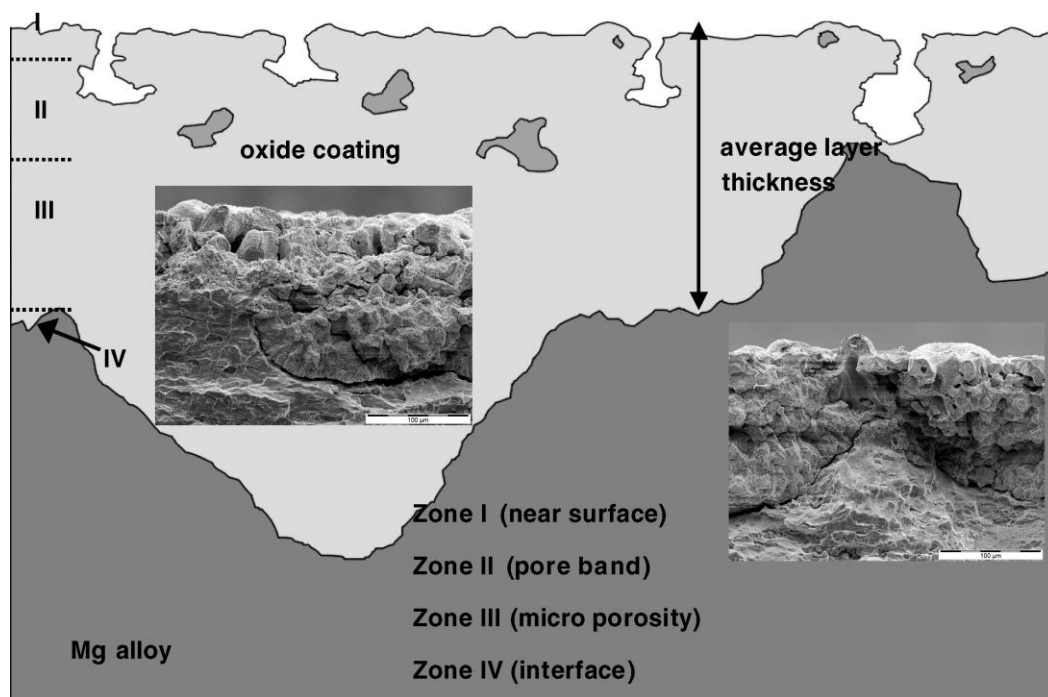
Figure 2-6 Schematic diagram of typical cross-sectional features of the PEO coatings; inserted are SEM micrographs showing typical features of the surface layer. [66]

2.3 Plasma spectroscopy

Plasma spectroscopy is considered as one of the best available diagnostics techniques used in plasma processing to measure the electron number density, temperature, and plasma compositions.

2.3.1 Visible and near-ultraviolet (NUV) spectroscopy

In the same way that we use visible light to diagnose the world around us with our eyes and brains as detectors and analyzers, we can use the light emitted from plasma as a tool to examine what is going on in the plasma. This is a vital step towards understanding and exploring the plasma and its interactions, a requirement for the continued development of the PEO process. If we are just observing the emitted light, then it is a passive technique, and our measurements will not disturb the plasma conditions. Most spectrometry is done in the visible part of the spectrum (optical spectrometry), because of the experimental inconvenience and additional expense of working at infrared or ultraviolet wavelengths. Optical spectrometers are relatively inexpensive and widely available commercially. Analysis of observed spectra can, therefore, provide information on transitions and energy levels, providing a useful tool to determine various quantities of the emitting source. With the addition of atomic and molecular physics concepts and models, parameters such as electron temperature and density can be determined to make visible spectroscopy a sensitive diagnostic tool for plasmas.

Spectroscopy is an umbrella term covering the experimental observation, investigation, and analysis of electromagnetic radiation spectra. Visible and near-ultraviolet (NUV) spectroscopy is concerned with the observation and analysis of the spectra of radiation with Visible and NUV wavelengths. Visible and NUV light is emitted from plasma due to transitions between energy levels in the atoms, ions, and molecules of the plasma. The wavelength of the radiation is equal to the energy change and hence characteristic of the levels and interactions involved. Optical emission spectroscopy (OES) is the analysis of light that is emitted from a medium in the absence of external optical excitation. Significant levels of such optical emission (OE) are present only in special circumstances.

Figure 2-7 illustrates the emission process. Gaseous plasma species are elevated to excited states by collision with energetic electrons. As a species drops to a lower energy state, an electromagnetic wave is released. Since only excited species can release electromagnetic waves, the observed spectrum reveals the density of particles in the excited states, which is only a small fraction of the total particles, on the order of 10^4. Also, the spectrum can contain emission from intermediates and products that may overlap with that from the intended diagnostic species. As a result, it is necessary to choose selectively from the spectrum for the wavelength in performing diagnostics. We need to choose the wavelengths that are correlated with the diagnostic parameters.
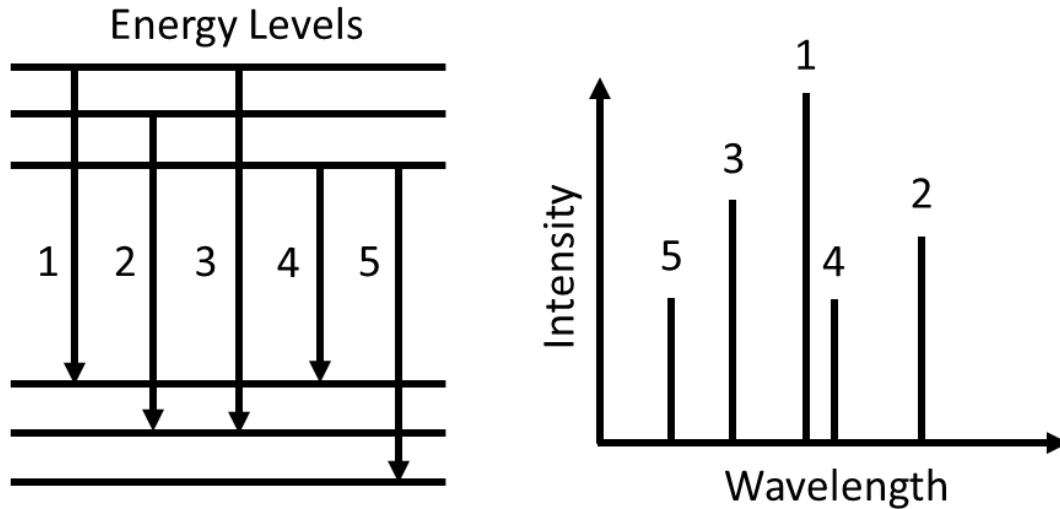
Figure 2-7 The energy levels involved in typical OES experiments.

Optical emission in the plasma chamber is collected by the lens, transmitted through an optical fiber, imaged onto the entrance slit, and dispersed by the diffraction grating system. Then an ICCD camera detects the dispersed beam through the exit slit. The diffraction grating is usually a square. The grating equation is:

$$m\lambda = d(sin\theta_m - \theta_i) \quad (2.1)$$

Where m is the diffraction order, d is the groove separation distance, and θ_m and θ_i; are the angles of incidence and diffraction, respectively. The grooves are designed to maximize the first-order diffraction (m=l) at a particular wavelength. The wavelength resolution of dispersion can be computed as:

$$\Delta\lambda = \frac{w}{mvf} cos\theta_m \quad (2.2)$$

Where w is the exit slit width, f is the spectrometer focal length, which is the distance from the exit plane to the last focusing mirror, v is the groove density.

2.4 Recent developments on the PEO coating

Recently, extensive studies have been carried out aiming at obtaining high quality PEO coatings on Mg and its alloys, which are capable of improving corrosion and wear resistance in large scale manufacturing. These exciting researches not only provide an idea for producing high quality PEO coatings but can also inspire future research and development.

The process optimization has always been of interest in PEO related research. Various approaches have been tried to obtain PEO coating with improved integrity and properties, including using the different power supply, auxiliary gas, and ultrasonic power, etc. Since the discharge activity plays a vital role in the electrochemical and thermal reactions, which are the critical factors affecting coating properties, such as phase composition, microstructure, and stress state, considerable investigations of discharge phenomena have been carried out in recent years [43, 72-79].

Yerokhin et al. [65] investigated the discharge phenomena during the PEO process on Al-alloy. According to their research, the discharge population is dominated by small-sized events throughout the oxidation process, with a proportion of only 11% medium-sized and 12% large discharge at the end of the PEO process. The cross-sectional area of a single discharge can reach up to 1.35 mm^2. More importantly, a new discharge model is suggested according to the glow discharge electrolysis theory, which explains some discharge characteristics that cannot be fitted into existing models (e.g., dielectric breakdown and discharge-in-pore). The discharge temperature was also studied widely, which is estimated in a range of $800 - 20000$ K depending on particular discharge activities [32]. The individual discharge lifetime has also been studied broadly by various research methods; it is proven to be in a range of tens to hundreds of microseconds. Moreover, in the PEO process, more than one species would be ionized at different stages, which is the main reason for the change in discharge color.

Gao et al. [80] studied Ca- and P-containing PEO coatings on Mg produced at pulsed unipolar power mode. According to their result, the PEO coating produced at 3000 Hz pulse frequency showed the best corrosion resistance performance compared with those produced at other frequencies. Nominé et al. [81] have reported the effect of cathodic half-period on the discharges and microstructure of PEO coating on Mg alloys. It was claimed that the discharges become shorter and smaller with the increase in the cathodic half-period, which accelerates the coating growth rate, enhances compactness, as well as corrosion resistance. This result is in good agreement with others [82-83].

Moreover, the effect of ultrasonic power on the microstructure and properties of the PEO coating on Mg alloys was also studied by Guo et al. [84]. It was found that the ultrasonic power at a constant frequency of 25 kHz and 400 W can effectively enhance the growth rate of PEO

coating, probably due to the accelerated rate of mass transfer in the coating. It also has a significant influence on the formation of microstructure and the distribution of chemical elements in the coating during the PEO process. However, no changes in the coating phase composition could be found following the ultrasonic power-assisted PEO process. It is important to note that optimal parameters for the PEO treatment are subject to the working conditions, and vary significantly depending on substrate materials and electrolytes.

Stojadinovic et al. [85] demonstrated luminescence phenomena during anodization of Mg-alloy AZ31 in water solution. The plasma time and spatial distribution on the sample surface analyzed using real-time imaging. The spatial density of micro discharges was the largest after about 80 s from the beginning of the PEO process. It reduces considerably during the next 200 s and later stays almost constant. The percentage of oxide coating area covered by active discharge sites was maximum after about 120 s and then stay roughly constant. Arrabal et al. [15] characterized AC PEO coating on Mg-alloys using OES and fast video imaging. They found initiation and gradual increase in the number of discharges after 2-4 ms of each anodic pulse once critical voltage reached. However, a cathodic half pulse did not show discharges. Wang et al. [86] studied discharge mechanism and plasma characteristics in different electrolytes. They concluded that the bubble layer breaks initially (at the oxide-electrolyte interface), followed by a breakdown of the dielectric barrier layer. Also, active plasma species were mainly composed of metal atoms and gas elements. All of which goes through dissociation, ionization, and excitation. Hussein et al. [42, 87] demonstrated the temperature measurement using H_α and H_β emission lines. They studied the effect of current mode on discharge type and plasma temperature and found that the application of pulsed bipolar current resulted in high spike peaks on temperature profiles. Therefore, they conclude that appropriate controlling of the positive to negative pulse current ratio, and their timing could eliminate the high-intensity plasma discharges during the PEO process and hence improved coating quality. The discharge characteristics are dependent on electrolyte chemistry, processing parameters, as well as the composition of the sample material. The mechanisms underlying discharge events and their influence on the coating formation are still an open question in PEO related research, which requires further investigation. The studies of these typical phenomena can help in better understanding the principles and mechanisms of the PEO process, which could provide a possible theoretical basis for optimizing coating properties.

Chapter 3

Experimental Details and Analytical Techniques

In this chapter, the experimental procedures, material, and measurement procedures used in this study are described.

3.1 Experimental

3.1.1 Sample (anode) and counter electrode (cathode)

AZ91D magnesium alloy was chosen as a sample material for the PEO coating process. Table 1 shows the composition of AZ91D Mg-alloy. Figure 3-1 shows the anode and cathode drawing used in this study. The square samples with dimensions of 30 mm x 30 mm x 8 mm were cut from sheet material. The samples were manually ground and polished on 180, 360, 600, 1000, 1500 grit silicon carbide (SiC) waterproof abrasive papers to obtain a uniform surface roughness. Further, the sample was cleaned using an ultrasonic cleaner for 300 s and dried with warm air before the PEO process. Two stainless steel plates with a dimension of 60 mm × 60 mm × 5 mm and a hole of 16 mm at the center was used as counter electrode and fixed at a distance of 30 mm in either side of the sample. The hole to the counter electrode is made for optical emission measurement.
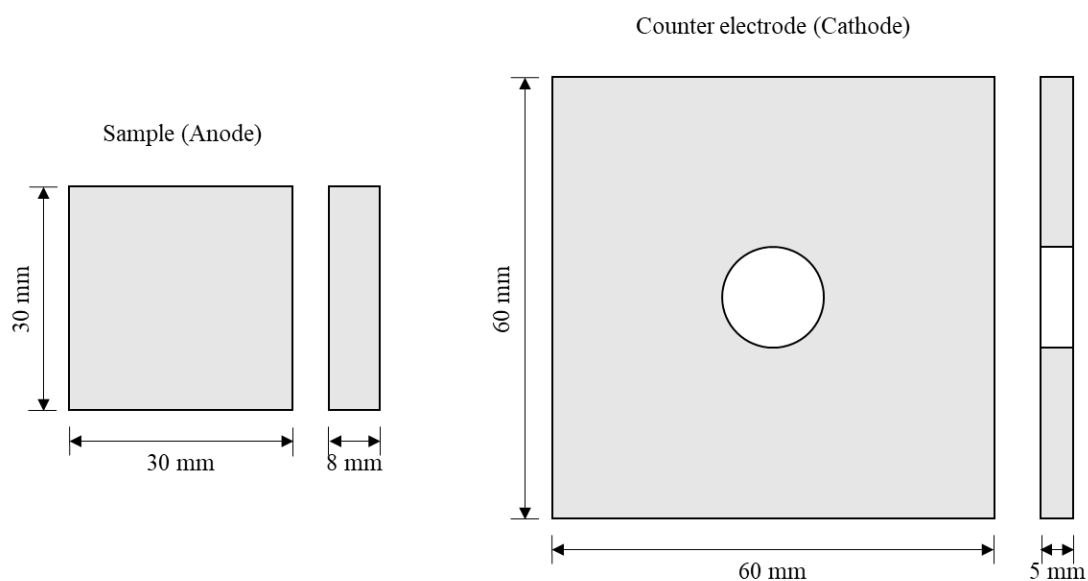
Figure 3-1 Drawing of a sample (anode) and counter electrode (cathode) used during the PEO of AZ91D Mg-alloy.

Table 3-1

Composition of AZ91D Magnesium Alloy

AZ91D Magnesium alloy composition (wt. %)

Al	Zn	Mn	Si	Cu	Fe	Mg
9.22	0.51	0.20	0.025	0.006	0.002	Balance

3.1.2 Electrolyte solution

The PEO coating was prepared in an electrolyte containing potassium hexafluorozirconate (K_2ZrF_6) as an additive. This is because of the solubility of the K_2ZrF_6 increase with temperature. However, it shows finite solubility in a high pH environment. Moreover, it was reported that fluoride helps to improve the corrosion resistance of the PEO coatings on magnesium [88-89]. Therefore, sodium fluoride (NaF) was used to maintain a pH of electrolyte at 11.6 for each experiment. The solution was continually circulated across the sample surface using the pump and passed through the cooling system, which was maintained at 293 K. Table 3-2 shows the composition of the electrolyte solution. The electrolyte solution was made by mixing the chemicals in series, as shown in Table 3-2. The pH of electrolyte was measured using PH-0611A meter, which can measure pH from 0.00 to 14.00 with a resolution of 0.01 pH.

Table 3-2

The composition of an electrolyte solution

Chemical powder	Weight for 1 L solution (g)
DI water	base
K_2ZrF_6	1
$(NaPO_3)_6$	5
NaF	1.5
NaOH	1

3.1.3 Power Supply

The bipolar current mode, comprising two components, i.e., the positive component and negative component, was used during the PEO process. In each pulse, the pulsed current reached its maximum, after which it remains constant for the ON-time of each pulse. The power supply was specially designed to allow independent control over the main pulse parameters, such as pulse duration, amplitude, and duty cycle, during both positive and negative biasing using a SPIK2000A-03 controller. The pulse unit SPIK2000A-03 can be operated in many modes (Bipolar, Unipolar, DC- and DC+ modes) with pulse duration (the ON and OFF times) being freely adjustable from the five µs per pulse unit range to the 32 ms per pulse duration range (30 Hz to 50 kHz).

A constant current bipolar pulse mode with a frequency of 500 Hz and a duty ratio of 10 % was set for each set of experiments. Figure 3-2 shows the applied constant current bipolar pulse waveform to the anode, and respective values are mentioned in Table 3-3. Two different cases by changing anodic to cathodic current ratio; less than one and greater than one at the same frequency and duty ratio was studied to understand the effect of current density on plasma emission during the PEO process. Equation (3.1) and equation (3.2) were used to calculate the frequency and duty ratio of applied power supply. Since the conductivity of the oxide film decreases with the increase of coating thickness, the input voltage between anode and cathode has to increase gradually to maintain the current density. Voltage increment versus treatment time was recorded for each sample.

$$Frequency\ (Hz) = \frac{1}{T_{ON}^+ + T_{OFF}^+ + T_{ON}^- + T_{OFF}^-} \quad (3.1)$$

$$Duty\ Ratio\ (\%) = \frac{T_{ON}^+}{T_{ON}^+ + T_{OFF}^+ + T_{ON}^- + T_{OFF}^-} \quad (3.2)$$

Where T_{ON}^+ is positive charge supply on time, T_{OFF}^+ is positive charge supply off time, T_{ON}^- is negative charge supply on time and T_{OFF}^- is a negative charge supply off time to the sample.

Table 3-3

PEO process parameters

Case	Bipolar pulse timing (µs)				Frequency (Hz)	Duty Ratio (%)	Anode Current (A)	Cathode Current (A)	Current Ratio (-)
	Anodic pulse		Cathodic pulse						
	T_{ON}^+	T_{OFF}^+	T_{ON}^-	T_{OFF}^-					
I	200	800	200	800	500	10	1.2	1.0	1.20
II	200	800	200	800	500	10	1.5	1.7	0.88
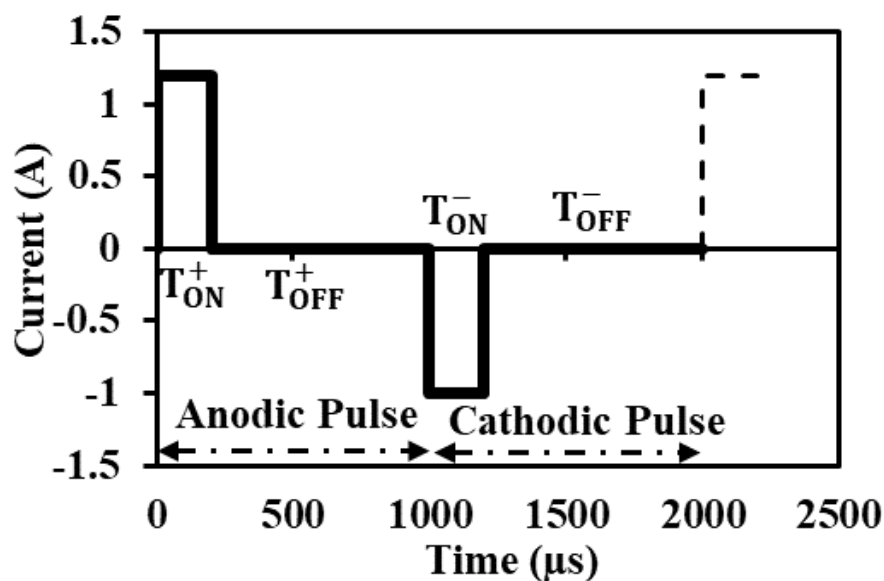
Figure 3-2 Applied constant current bipolar pulse waveform to sample during the PEO of AZ91D Mg-alloy.

3.2 Solution transmission measurement

The cathodes were fixed 30 mm away to the sample on both sides, with flowing electrolyte in between them for the cooling purpose. Therefore, neglecting the solution transmission effect can lead to a considerable error in measured plasma emission intensity. The solution during the oxidation reaction was taken out at every 600 s of interval. Figure 3-3 shows the schematic of the experimental setup for solution transmission measurement using the standard light (Stellar Net, SL1-CAL). The measurement cell made of glass was covered on both sides by black sheets to ensure the light should not pass to optical fiber from outside of the cell.
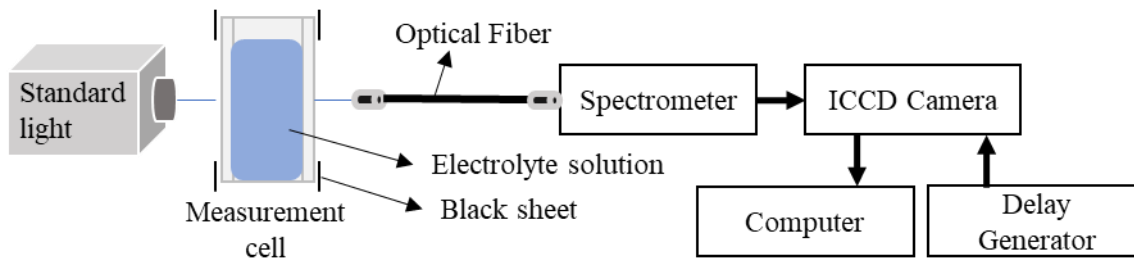
Figure 3-3 Schematic of the experimental setup for measurement of light transmittance of an electrolyte solution.

The light was transmitted through measurement cell have a thickness of 10 mm. Further, the light was transmitted using 600 μm core diameter optical fiber, which was screwed to the entrance slit of the spectrometer (Japan Spectroscopic Co. Ltd.). The entrance slit of the spectrometer was set to 20 μm in width. The grating of 300 grooves per mm was used for observing a wide spectral range from 480 nm to 880 nm. The spectrometer was attached to the thermoelectrically cooled ICCD camera (Princeton Instruments). The computer recorded the detected signal.

According to Lambert-Beer's law, when light permits a transmission medium, the strength of permitted light is related to absorber concentration. The transmission for 30 mm of path length was calculated using equation (3.3). [90] Considering electrolyte flow during the oxidation process, the solution was continually stirred during transmission measurement.

$$\frac{I_\lambda}{I_{\lambda 0}} = \exp\{-A_\lambda\} \quad (3.3)$$

Where $I_{\lambda 0}$ is incident light intensity, I_λ is transmitted light intensity, A_λ is absorbance.

3.3 The plasma emission measurement

Figure 3-4(a) and 3-4(b) shows the schematic of the experimental setup and optical arrangement for average plasma emission measurement using a photodetector, respectively. Average plasma emission was measured to understand the time of plasma emission within the power supply pulse. Figure 3-4(c) shows the optical arrangement used for spatial and time resolved optical emission measurement using the ICCD camera. The emitted plasma light was transmitted and focused through a quartz window of diameter 11 mm. Plasma emission light was collected using two plano-convex lenses, having 45 mm of focal length and 9 mm in

diameter. The convex side of both lenses was facing each other at a distance of 20 mm. Focused light was filtered using a long-pass 525 nm filter of 10 mm diameter (Edmund optics) to neglect reflected light because of the grating. The measured light was transmitted using 600 μm core diameter optical fiber, which was screwed to the entrance slit of the spectrometer (Japan Spectroscopic Co. Ltd.). The entrance slit of the spectrometer was set to 20 μm in width. The grating of 300 grooves per mm was used for observing a wide spectral range from 480 nm to 880 nm. The spectrometer was attached to the thermoelectrically cooled ICCD camera (Princeton Instruments). The computer recorded the detected signal. The delay generator controlled the time between a power supply for a cathode, anode, and an ICCD camera. The system calibration was carried out before the experiment using the standard light (Stellar Net, SL1-CAL).
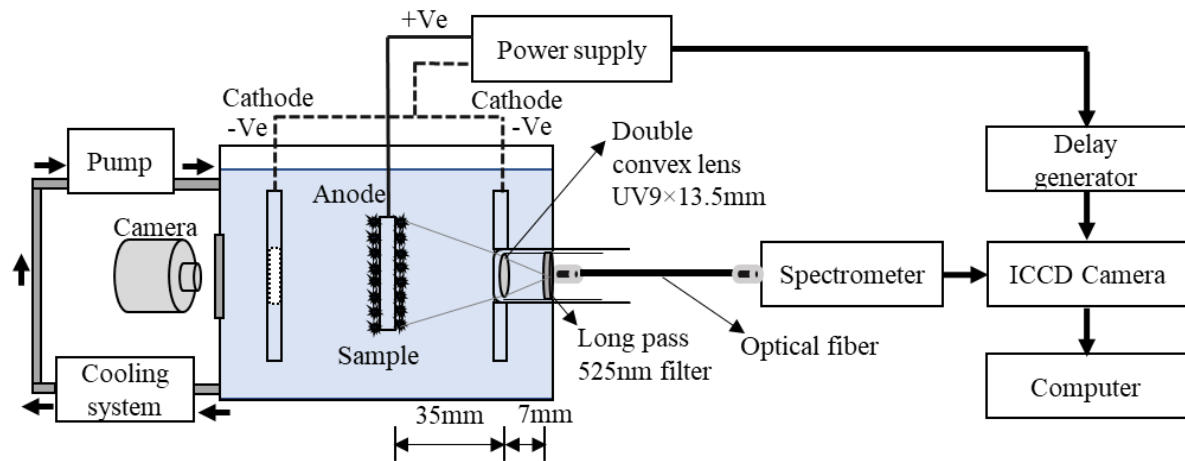
(a) Schematic of the experimental setup for light emission measurement using spectrometer and ICCD camera during the PEO of AZ91D Mg-alloy.
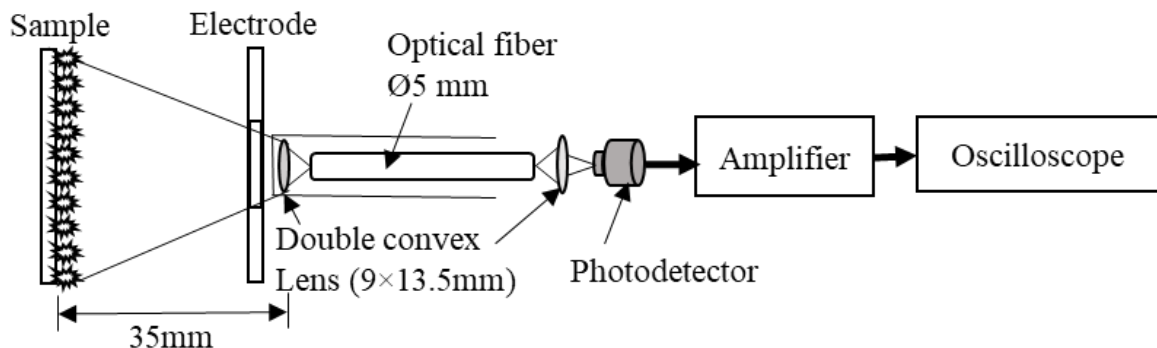
(b) Schematic of optical arrangement used for plasma emission measurement using a photodetector during the PEO of AZ91D Mg-alloy.
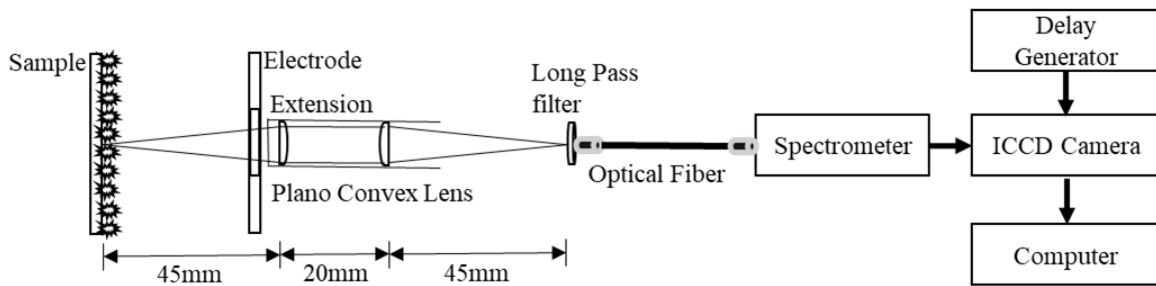
(c) Schematic of optical arrangement used for spatially and time-resolved optical emission measurement using spectrometer and ICCD camera during the PEO of AZ91D Mg-alloy.
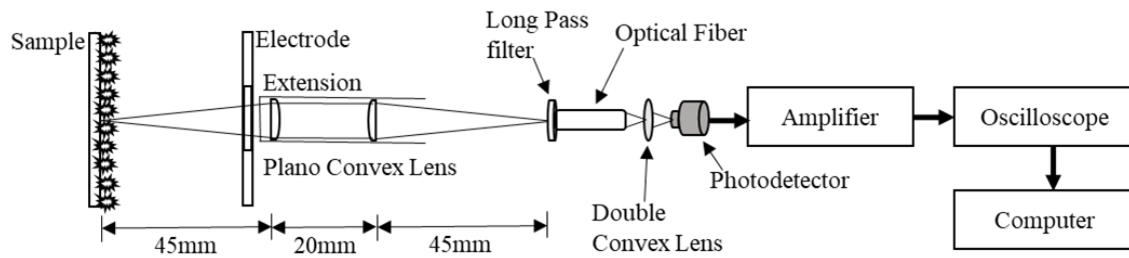
(d) Schematic of optical arrangement used for spatially resolved emission measurement using a photodetector during the PEO of AZ91D Mg-alloy.

Figure 3-4 Schematic of the experimental setup for emission measurement during the PEO of AZ91D Mg-alloy.

Figure 3-4(d) shows the schematic of the optical arrangement used for emission measurement using a photodetector (Hamamatsu photonics, S1336-44BQ). The spectral response range of photodetector was 320 nm to 1100 nm. The same lens setup was used, as explained above. The optical fiber of a 5 mm core diameter was used to transmit light to photodetector through a double convex lens having a 13 mm focal length and 9 mm diameter. The distance between optical fiber end, double convex lens, and photodetector was fixed to collect maximum light. The photodetector signals were monitored simultaneously with the bipolar pulse voltage to sample. The signal was recorded by a four-channel pico-scope at 100 ms/div sampling rate and 16-bit vertical resolution after amplifying it using a 2 MHz amplifier (Cosmo-wave, FP002MSA-10db).

Chapter 4

Experimental results and discussion I: Plasma stability, spatial and time resolution

In this chapter, the effect of different processing parameters on plasma stability is discussed with an evaluation of spatial resolution and time resolution for emission measurement.

4.1 Plasma stability

The stability of plasma is an essential consideration in the study of plasma emission behavior or plasma physics. The PEO process was repeated several times to achieve the plasma stability. It was found that the appearance of plasma during the PEO process depends on many factors such as electrical charge applied to anode and cathode, bipolar pulse time, pH of the electrolyte solution, and others. In this study, the aim is to study time dependent plasma emission behavior during the PEO process, which required the plasma emission to be continued during the PEO process time. However, it was found that plasma disappears after some time of the process and no light emission to measure and study plasma emission behavior. Therefore, the PEO experiment was repeated several times before getting a continuous plasma emission. Table 4-1 shows the experimental parameters for a trail of plasma stability. During these experiments, plasma emission was monitored using a camera, and also anodic voltage was monitored, respectively. The effect of changing bipolar pulse timing, current ratio, and series of the addition of chemical while making electrolyte solution and hence the pH was studied towards plasma stability. Table 4-2 shows the chemical composition for electrolyte solution for respective PEO experiments in Table 4-1. Each case of parameters was repeated to confirm plasma emission stability.

Figure 4-1 shows the typical output voltage change during the PEO process for different working conditions, as mentioned in Table 4-1. The output voltage directly relates to plasma emission during the PEO process. From the measured results, the output voltage was divided into three steps as "arc regime," "Voltage breakdown," and "soft regime." The arc regime defines the appearance of intense plasma during the process, voltage breakdown defines the sudden drop of voltage during the process, and a soft regime defines the no arcing during the

process. These three happenings during the PEO process can be determined by voltage conditions, as mentioned in Table 4-3.

Table 4-1

PEO process parameters studied for plasma stability

Case	Bipolar pulse timing (µs)				Anode Current (A)	Cathode Current (A)	Current Ratio (-)	pH before	pH after
	Anodic pulse		Cathodic pulse						
	T_{ON}^{+}	T_{OFF}^{+}	T_{ON}^{-}	T_{OFF}^{-}					
1	200	850	100	850	1.0	1.2	0.83	11.6	11.5
2	200	850	100	850	1.0	1.2	0.83	11.5	11.5
3	200	750	300	750	1.0	1.2	0.83	11.4	11.4
4	200	750	300	750	1.0	1.2	0.83	11.3	11.1
5	200	750	300	750	1.0	1.2	0.83	11.1	11.1
6	200	750	300	750	1.0	1.2	0.83	11.0	11.0
7	200	750	300	750	1.0	1.2	0.83	11.6	11.5
8	200	800	200	800	1.0	1.2	0.83	10.1	9.9
9	200	800	200	800	1.5	1.7	0.88	11.6	11.6
10	200	800	200	800	1.2	1.0	1.2	11.6	11.6

Table 4-2

The composition of an electrolyte solution used for plasma stability

Case	Chemical powder	Weight for 1 L solution (unit)
1, 2, 3	DI water	Base
	$(NaPO_3)_6$	5 (g)
	NaF	1.5 (g)
	ZSL-10A	20 (ml)
	NaOH	50 (ml)
4, 5	DI water	Base
	$(NaPO_3)_6$	5 (g)
	NaF	1.5 (g)
	K_2ZrF_6	1.0 (g)
	NaOH	50 (ml)

6, 7	DI water	Base
	K_2ZrF_6	1 (g)
	$(NaPO_3)_6$	5 (g)
	NaF	1.5 (g)
	NaOH	50 (ml)
8	DI water	Base
	K_2ZrF_6	6 (g)
	$(NaPO_3)_6$	5 (g)
	NaOH	170 (ml)
9, 10	DI water	Base
	K_2ZrF_6	1 (g)
	$(NaPO_3)_6$	5 (g)
	NaF	1.5 (g)
	NaOH	50 (ml)
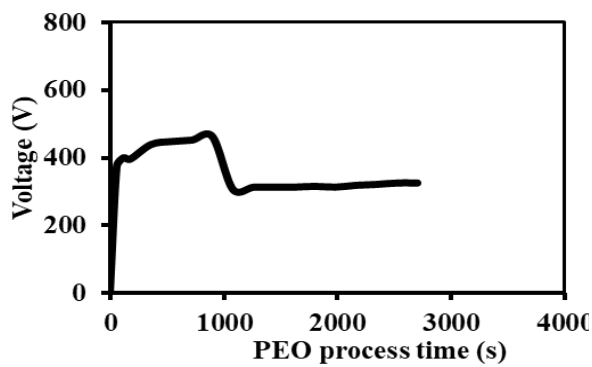
(a) Case 1
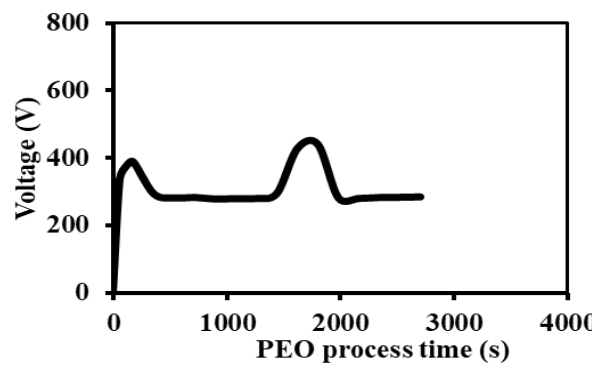
(b) Case 2
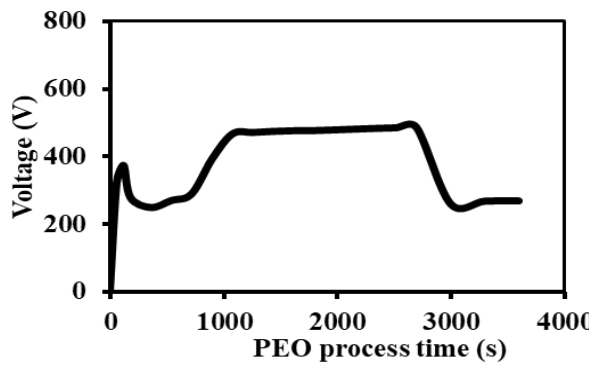
(c) Case 3
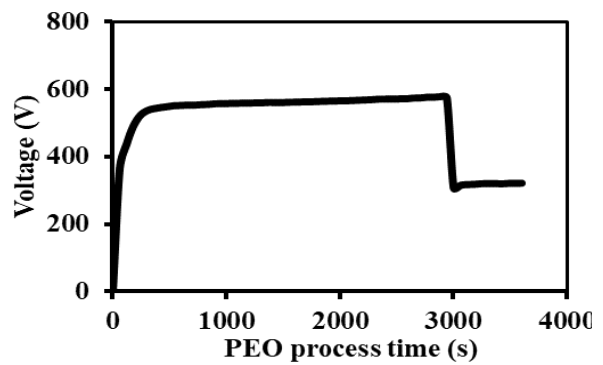
(d) Case 4
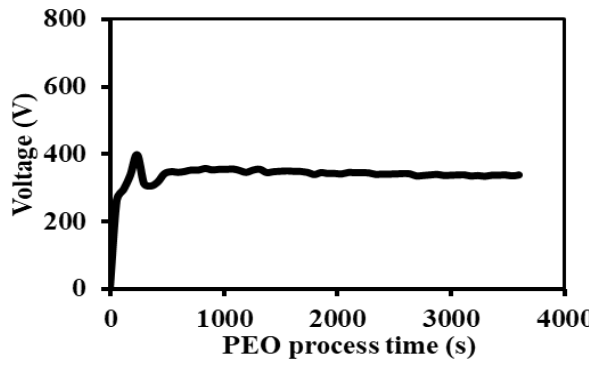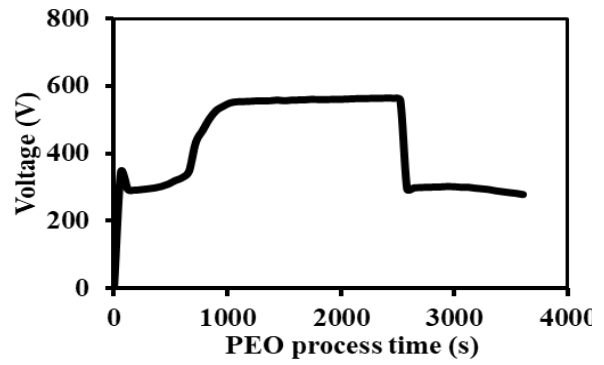
(e)   Case 5   (f)   Case 6
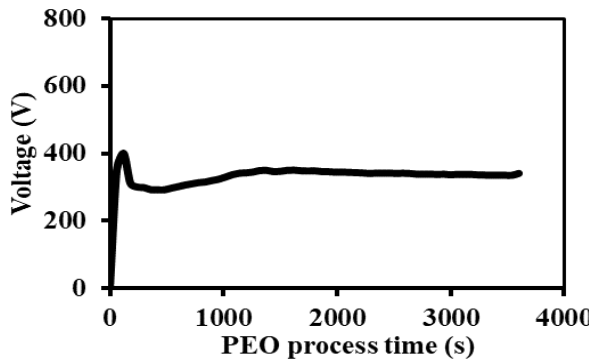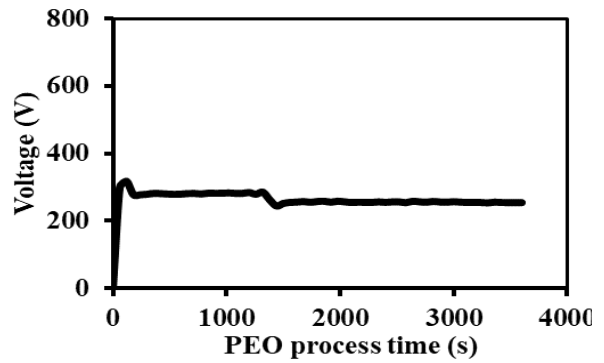
(g)   Case 7   (h)   Case 8
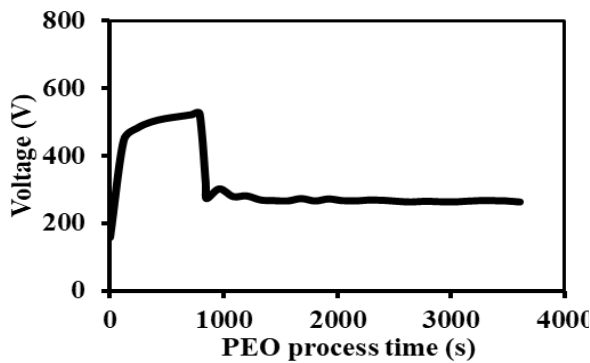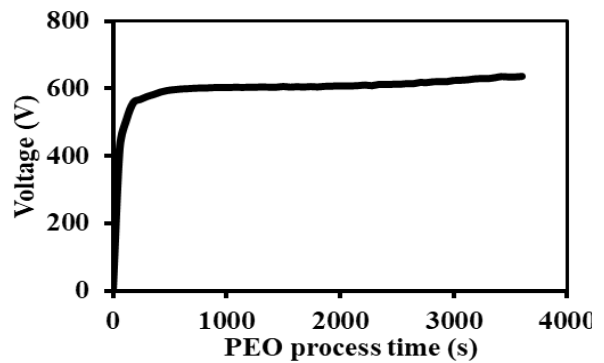
(i)   Case 9   (j)   Case 10

Figure 4-1 The typical anodic voltage response for different cases (table 4-1) during the PEO of AZ91D Mg-alloy.

From the measured voltage results, it was found that output voltage depends on anodic pulse time and applied anodic to cathodic current ratio. For case 1 and 2 input parameters as electrical parameters and composition of the electrolyte solution is same with constant pH. However, output voltage shows the different behavior with a time of the PEO process. Therefore, keeping

the same electrical parameters with different electrolyte solution case 3 was checked and found an unstable plasma appearance. The output voltage from case 4 shows the stable output voltage during the PEO process. However, with the same operating condition, case 5 does not show any plasma emission during the process.

Table 4-3

The mathematical definition of conditions to determine steps during the PEO process.

Sr. No.	Condition 1	Condition 2	Steps
1	$Y_1 > 300 \pm 10$ V	$Y_2 \leq 100 \pm 10$ V	Arc regime
2	$Y_1 \geq 300 \pm 10$ V	$Y_2 \geq 100 \pm 10$ V	Voltage breakdown
3	$Y_1 < 300 \pm 10$ V	$Y_2 < 100 \pm 10$ V	Soft regime

The voltage ratio and voltage difference ratio are defined as follows;

$$Y_1 = \frac{A_i^2 + C_i^2}{A_i + C_i} \quad (4.1)$$

$$Y_2 = \frac{(A_i - A_{i+1})^2 + (C_i - C_{i+1})^2}{(A_i - A_{i+1}) + (C_i - C_{i+1})} \quad (4.2)$$

Where A_i is anodic voltage, and C_i is a cathodic voltage at the particular time i.

Similarly, for the case 6-9 the plasma stability was not found. For the case of case 10, output voltage increasing with time and shows continuous arcing throughout the PEO process. Therefore, parameters of the case 10 were used for spatially resolved and time resolved emission measurement. However, input parameters, as shown in case 9, were also studied to understand the effect of current density effects on plasma emission behavior during the PEO process. Figure 4-2 shows the plasma images for case 10 at the interval of 240 s during the PEO process time. These images show that arcing is continue after 720 s until the end of the PEO process.

(a) 240 s   (b) 480 s   (c) 720 s

(d) 960 s   (e) 1200 s   (f) 1440 s

(g) 1680 s   (h) 1920 s   (i) 2160 s

(j) 2400 s   (k) 2640 s   (l) 2880 s
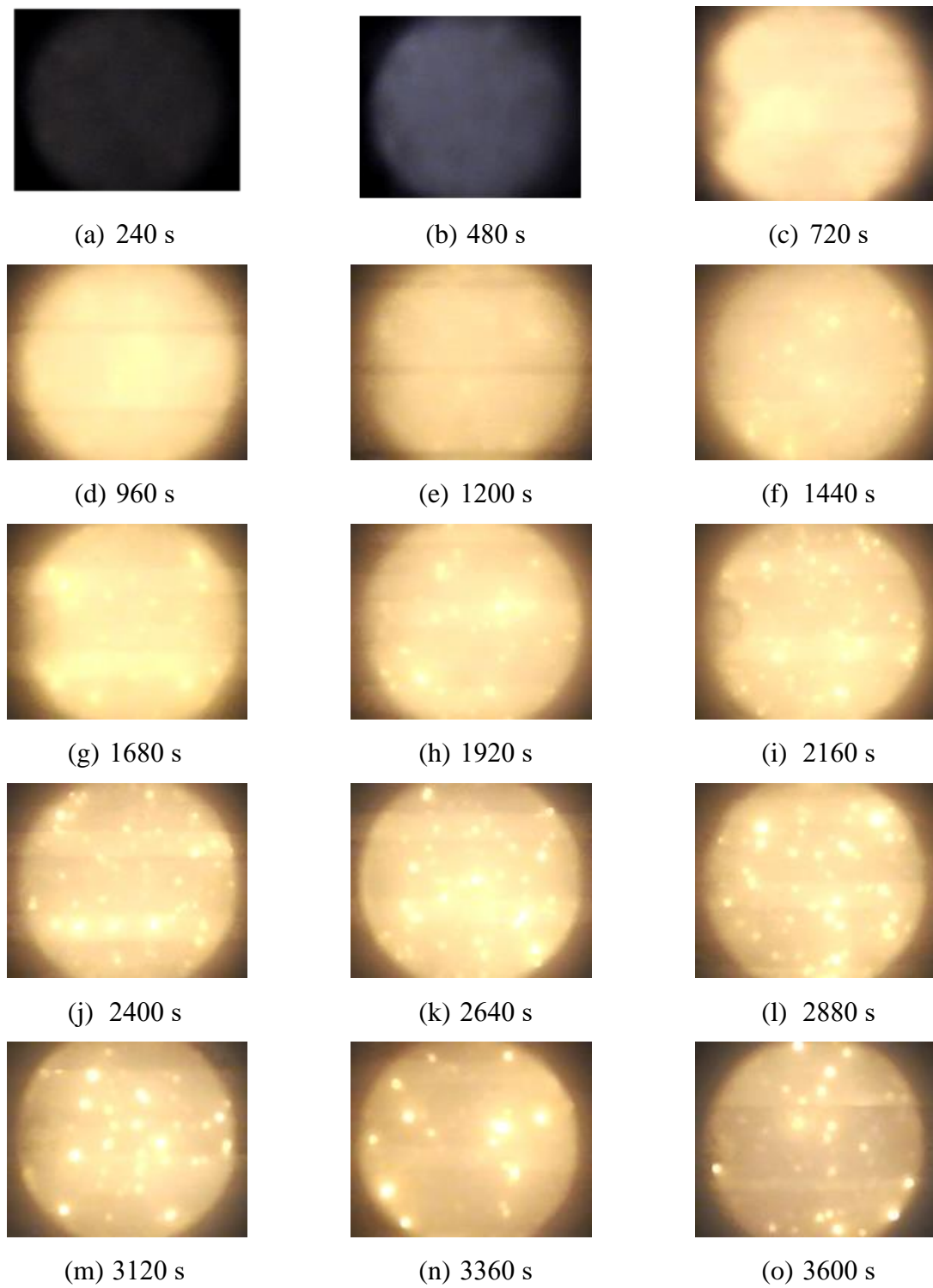
(m) 3120 s   (n) 3360 s   (o) 3600 s

Figure 4-2 The plasma images recorded by camera for case 10 at the interval of 240 s during the PEO of AZ91D Mg-alloy for 3600 s.

4.2 Evaluation of spatial resolution

It was essential to evaluate the light-emitting area size for deciding the spatial resolution. According to the best of our knowledge, it is the first time to report plasma size analysis during the PEO process on Mg-alloy. Images at 900 s, 1800 s, 2700 s, and 3600 s were taken from the recorded video by a camera, as shown in Figure 3-4 (a).

Before the experiment, an image area was measured using a standard scale. According to it, the range of 8 pixels/mm was set. The recorded image was converted to an 8-bit black and white format, as shown in Figure 4-3 (a). Next, to spot the bright area threshold was set to 220 for images at 900 s, 1800 s, and 230 for images at 2700 s, 3600 s. The threshold values were selected randomly. The pixel had an intensity of more than the threshold value highlighted by a red color. The highlighted area was the light emission area. Figure 4-3 (b) shows the histogram for the light emission area, where 52% area was less than 0.55 mm^2, 32% in the range of 0.55 mm^2 to 1.1 mm^2, and the rest 16% was more significant than it. From the results, a 90% light emission area was more prominent than 0.25 mm^2. Therefore, the spatial resolution of 0.25 mm^2 was decided for plasma emission measurement.
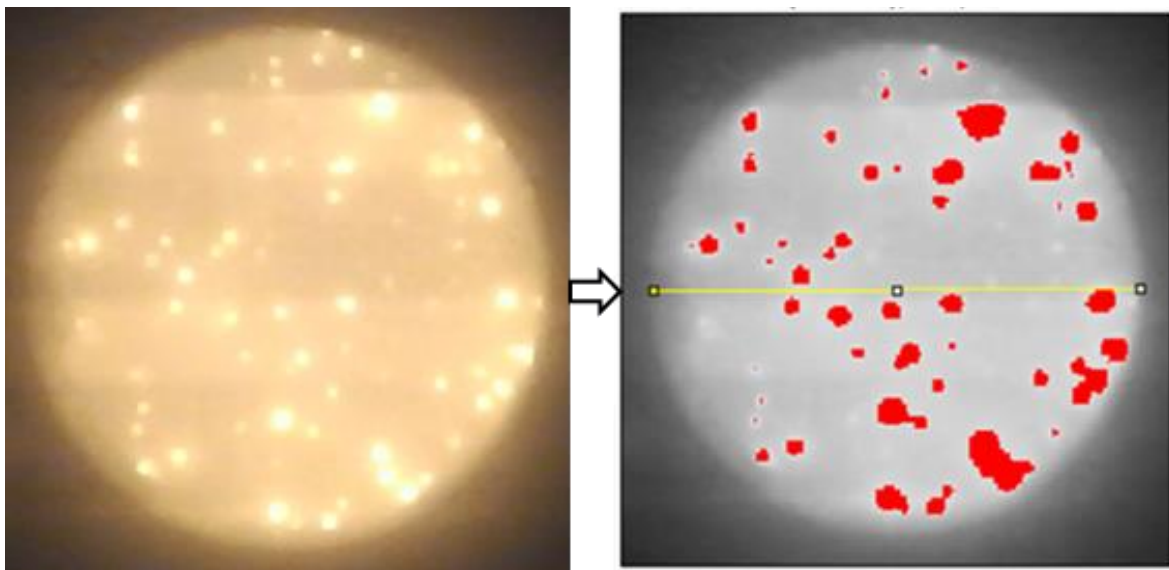
(a) The plasma image conversion to measure emission area size during the PEO of AZ91D Mg-alloy
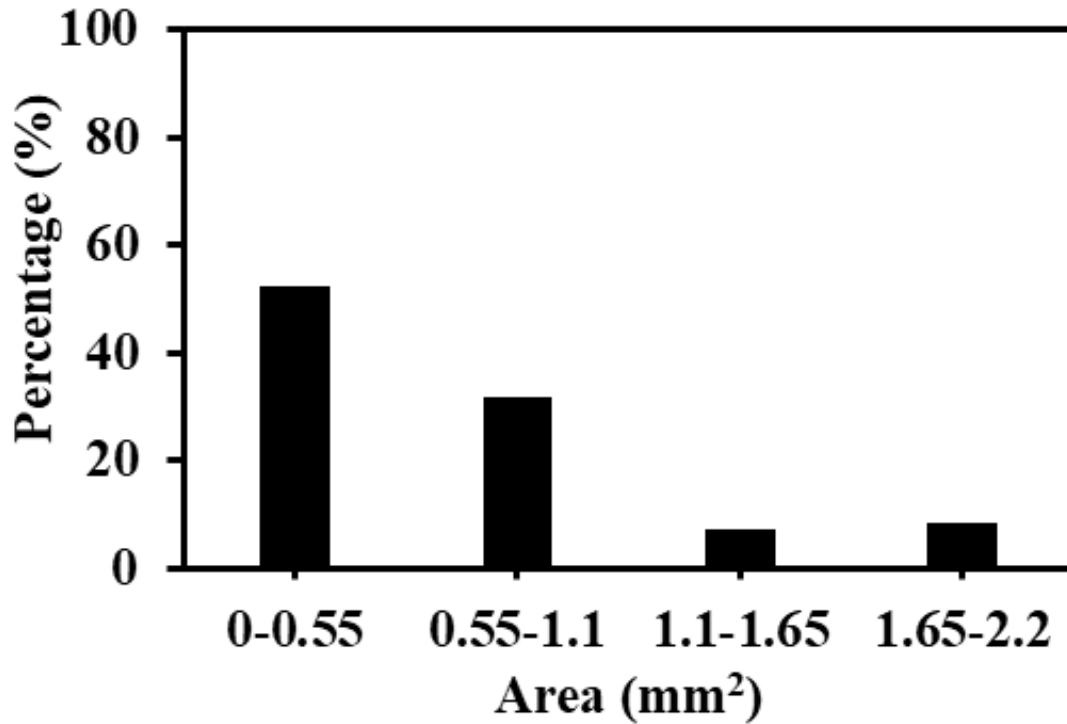
(b) Histogram of light emission area during the PEO of AZ91D Mg-alloy

Figure 4-3 Light emitting area during the PEO of AZ91D Mg-alloy using bipolar current mode.

4.3 Evaluation of temporal resolution

Before optical emission measurement using ICCD camera, plasma emission was monitored using a photodetector, as shown in Figure 3-4 (c). The emission was measured from 0.25 mm^2 of an area on the sample during a single anodic pulse, and Figure 4-4 (a) shows the sample spectrum. The baseline was created for the measured spectrum using a trendline function. The base-line was subtracted from the measured spectrum, and FWHM calculated for emission peak to get a plasma lifetime.

Figure 4-4 (b) shows the histogram for plasma lifetime during the PEO process. It shows that 46% of them have a plasma lifetime of smaller than 40 μs and 47% in the range of 40 μs to 80 μs. The rest had a lifetime of more than 80 μs. However, no plasma emission cycle was found with a lifetime of more than 160 μs for the pulse of 200 μs. Therefore, it was decided to have a time resolution of 20 μs for OES measurement using the ICCD camera.
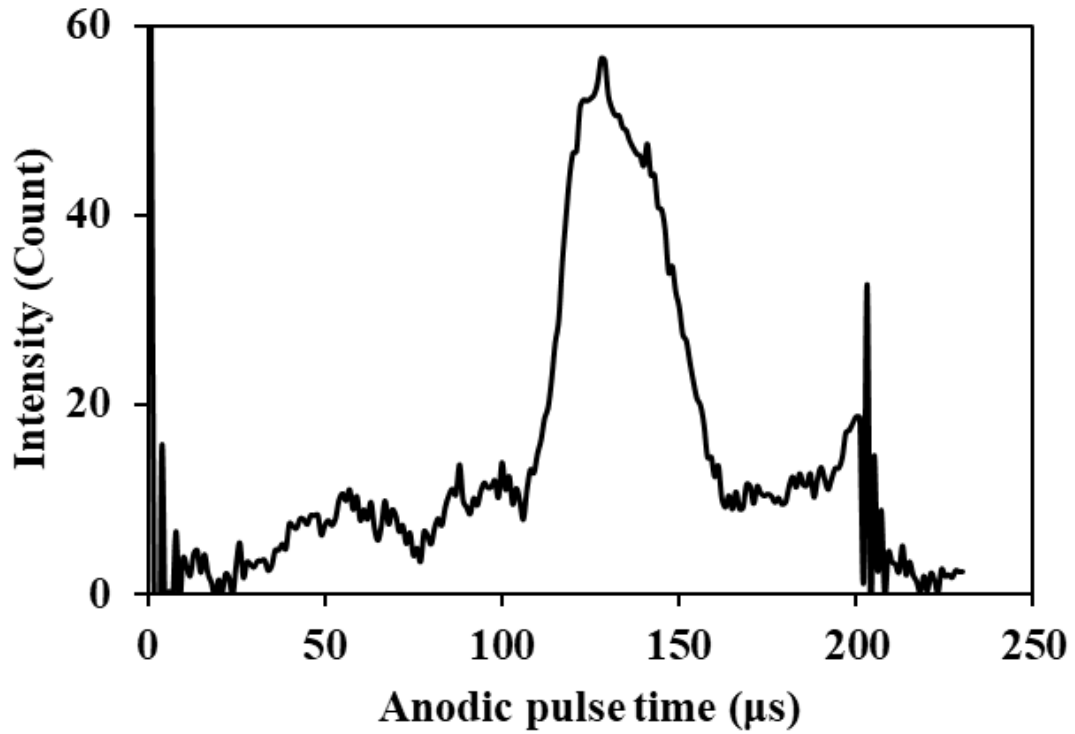
(a) The sample emission spectra at a spatial resolution of 0.25 mm^2 measured using a photodetector during the PEO of AZ91D Mg-alloy.
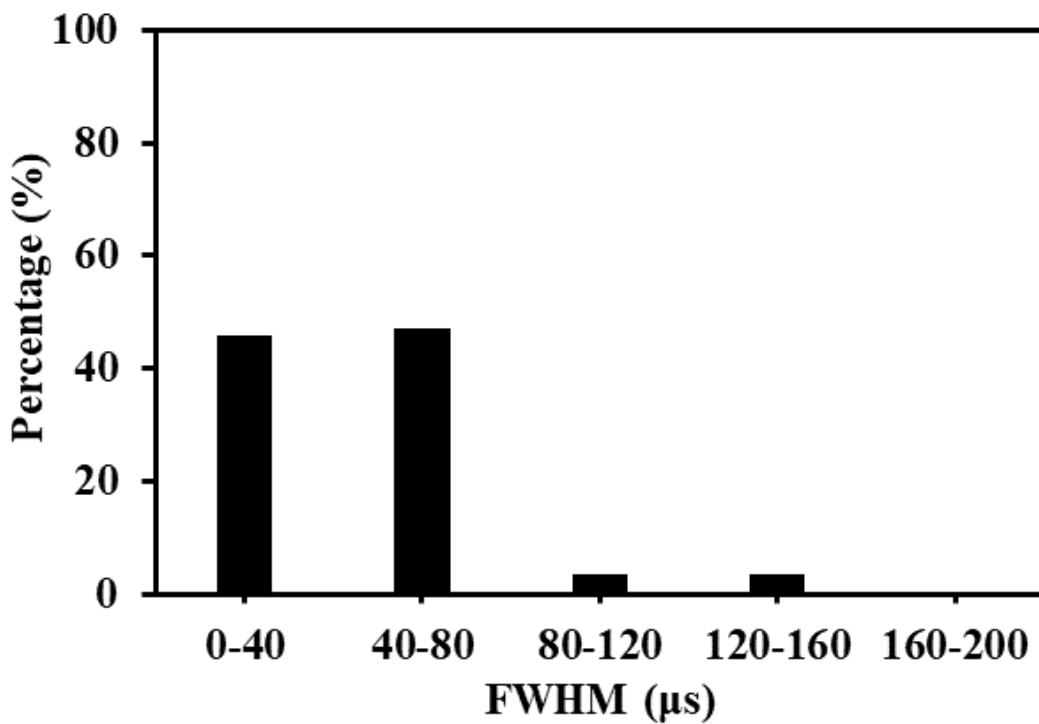
(b) Histogram of plasma lifetime during the PEO of AZ91D Mg-alloy

Figure 4-4 The plasma lifetime during PEO of AZ91D Mg-alloy using bipolar current mode.

Chapter 5

# Experimental results and discussion II: Spatial and time resolved emission results

In this chapter, plasma emission behavior with time is discussed using spatial and time resolved emission measurement approach. The change in plasma temperature with time is also discussed in this chapter.

5.1 Plasma emission measurement using a Photodetector

Figure 5-1 shows the measured output anodic voltage and average plasma emission for 100 bipolar pulse cycles concerning anodic pulse time at 900 s, 1800 s, 2700 s, 3600 s during the PEO process. Figure 3-4 (d) shows an optical arrangement used for this measurement. From the measured result, it was found that plasma discharge appears during an anodic pulse. Also, Arrabal et al. [15] confirmed that no discharges were observed during a cathodic half pulse. However, Nomine et al. [91] had reported the appearance of micro discharges in the early beginning of the cathodic half period also. But, the plasma emission during cathodic pulse was not seen in this measurement.

As shown in Figure 5-1, the measured output anodic voltage and plasma emission are divided into four steps according to happening during one anodic pulse. At the beginning of the anodic pulse, resistance is very high, which restricts the flow of current through the sample and the formed oxide layer. Therefore, a rapid increase in voltage and no plasma emission was seen initially. Once the voltage reaches its critical level, voltage breakdown happens, and resistance starts to reduce. Therefore, the current starts to flow in the second stage. In stage three, current flow through the micro-cracks or micro-holes on the oxide layer from an electrolyte to the sample surface, and due to the high voltage difference, a spark appears. In step four, resistance reduces continually until the end of the anodic pulse and respectively flow of current increase and hence the plasma emission. However, plasma emission behavior cannot be understood entirely because of the total emission measurement on the surface of the sample. Still, it can be said that most of the plasma discharge appears in the second half of the anodic pulse.
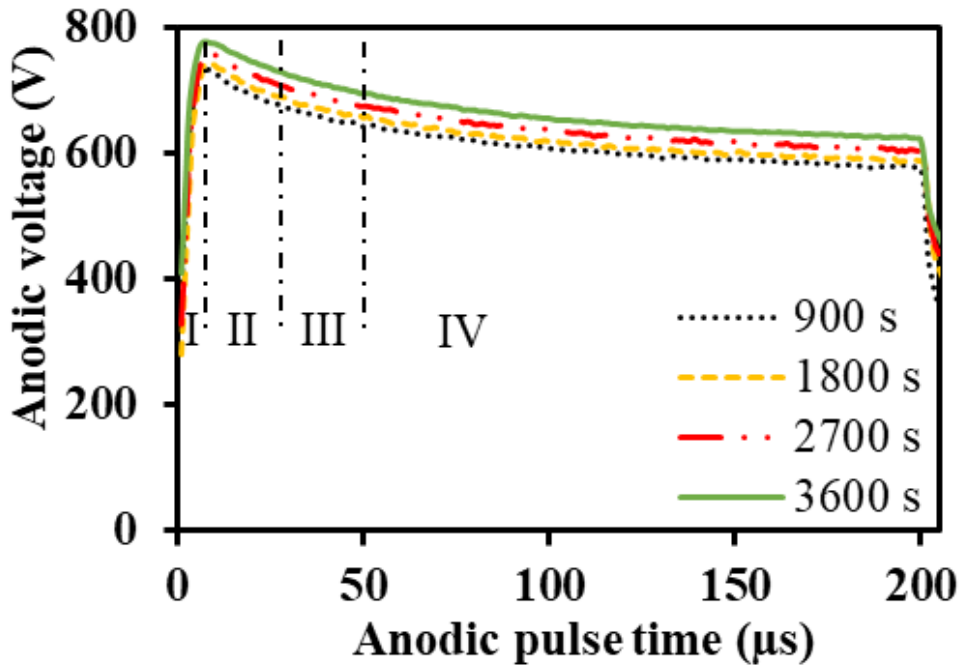
(a) Time dependence of anodic voltage during the PEO of AZ91D Mg-alloy using bipolar current mode.
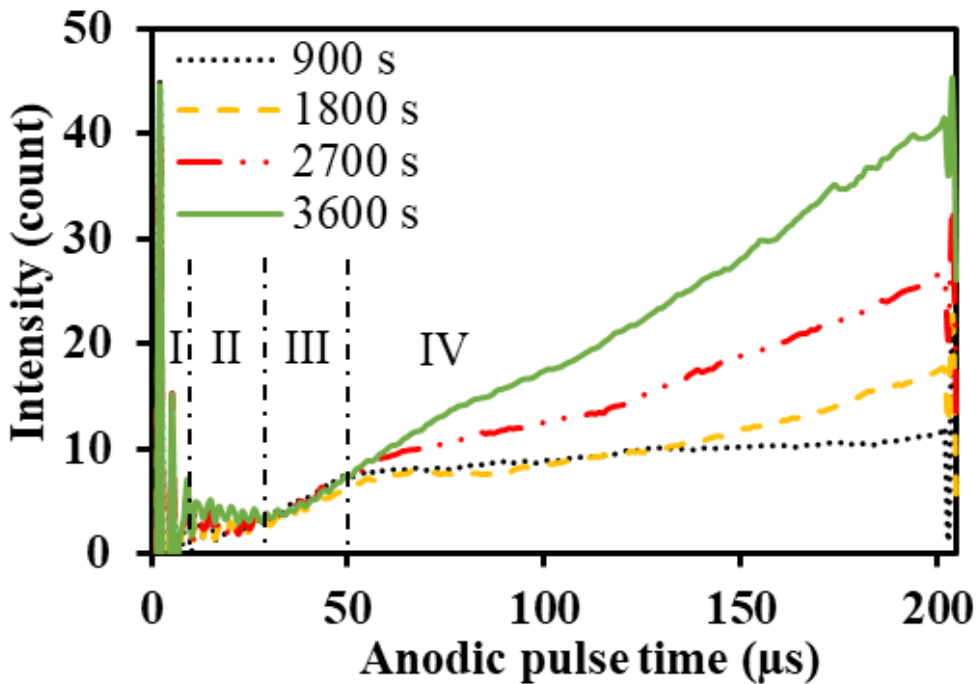
(b) Time dependence of measured plasma emission during the PEO of AZ91D Mg-alloy using bipolar current mode.
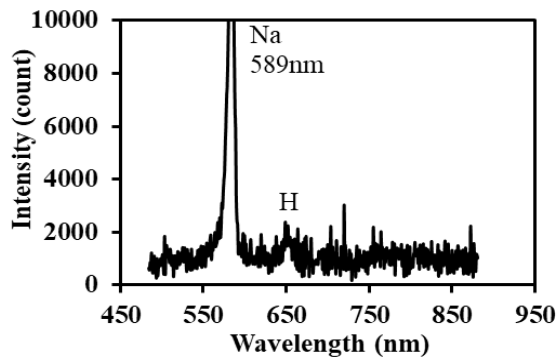
Figure 5-1 The time dependence of anodic voltage and measured plasma emission averagely for 100 successive cycles of an anodic pulse at 900 s, 1800 s, 2700 s, 3600 s during the PEO of AZ91D Mg-alloy using bipolar current mode.

Plasma shows the same emission behavior at the beginning of an anodic pulse throughout the PEO process. The ratio of average emission intensity during 180 μs - 200 μs to 110 μs - 130 μs was 1.0, 1.0, 1.7, and 1.8 for 900 s, 1800 s, 2700 s and 3600 s respectively. The ratio of average emission intensity at 1800 s to 900 s was 1.0 during 110 μs - 130 μs and 1.5 during 180 μs - 200 μs. However, the ratio of average emission intensity at 3600 s to 900 s was 2.2 during 110 μs - 130 μs and 3.6 during 180 μs - 200 μs. The emission intensity at 200 μs of an anodic pulse increases 1.6, 2.8, 3.5, and 5.4 times than at 50 μs for 900 s, 1800 s, 2700 s, and 3600 s, respectively. It implies that plasma emission intensity increases with applied voltage pulse time and also longer process time. Also, most of the strong emission intensity plasma appears during the second half of the anodic pulse.

5.2 Plasma emission measurement using an ICCD camera

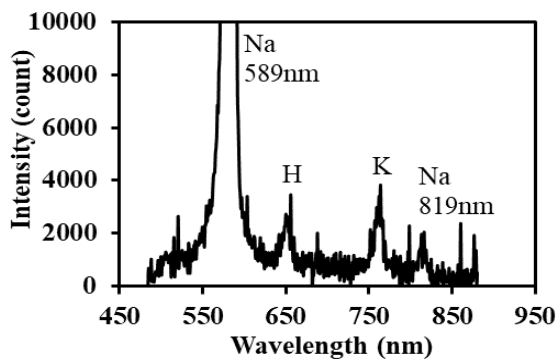### 5.2.1 Spatial and time resolved OES measurement

Figure 5-2 shows the typical spatial and time-resolved plasma emission spectra in near UV and visible region measured using an optical arrangement shown in Figure 3-4 (c). Emission measurement was carried out for a spatial resolution of 0.25 mm^2 and a time resolution of 20 μs. The measured plasma emission spectra contain sodium (Na-I) at 589 nm and 819 nm, hydrogen (H) at 656.27 nm, potassium (K-I) at 767.31 nm lines within the range of 490 nm to 890 nm. These are all from the electrolyte solution. From the measured results, it was found that emission spectra for the plasma after 130 μs of anodic pulse shows a non-uniform trend at a base. It results from bremsstrahlung radiation of electrons and collision radiative recombination [92-93]. As explained in section 3.3, plasma emission light was filtered using a long-pass 525 nm filter of 10 mm diameter (Edmund optics) to neglect reflected light because of the grating. Therefore, no emission line before 525 nm can be seen in the measured spectrum. However, for the emission spectra for anodic pulse time 170 μs – 190 μs, the Mg-I emission line can be seen. This is because the long-pass filter was not used during this experiment to check the atomic or ionic emission from other species. No effect was found on the atomic emission of Na-I line by the emission line of different species. From the emission spectra during the PEO process on AZ91D Mg-alloy, it was found that only Na-I shows the two emission lines at 589 nm and 819 nm withing a measured wavelength range. Also, Hussein et al. [94] mentioned that Na-I signals can be easily detected and can use as process monitoring parameters. Therefore, Na-I emission lines at 589 nm and 819 nm were used to study plasma behavior in terms of plasma emission and plasma temperature.

(a) Anodic pulse time 50 μs – 70 μs
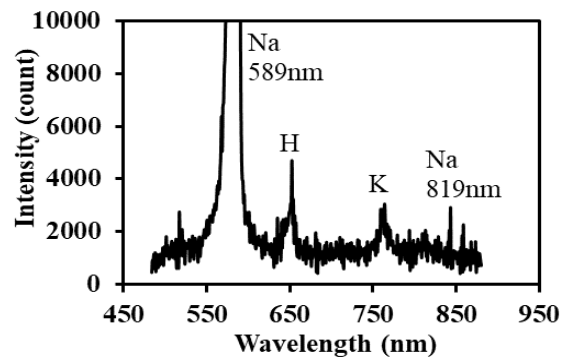
(b) Anodic pulse time 70 μs – 90 μs

(c) Anodic pulse time 90 μs – 110 μs

(d) Anodic pulse time 110 μs – 130 μs
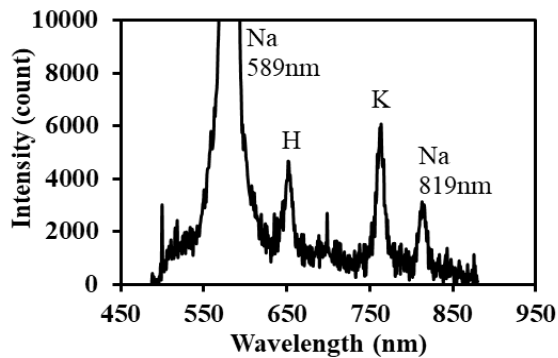
(e) Anodic pulse time 130 μs – 150 μs
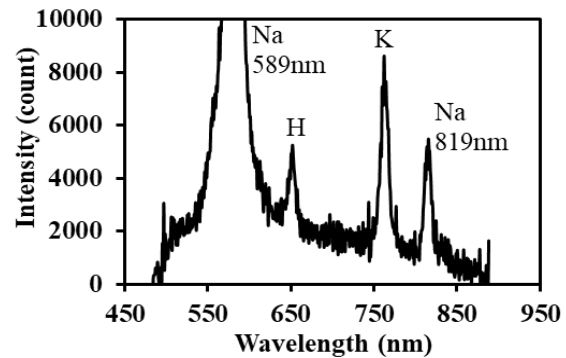
(f) Anodic pulse time 150 μs – 170 μs
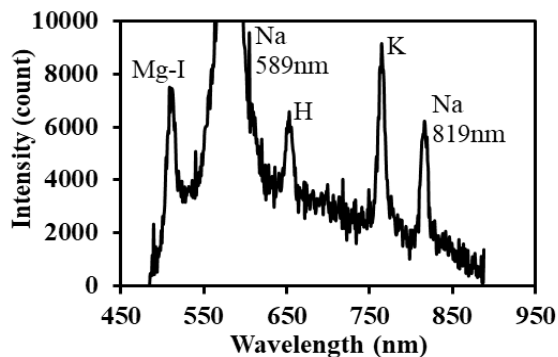
(g) Anodic pulse time 170 μs – 190 μs
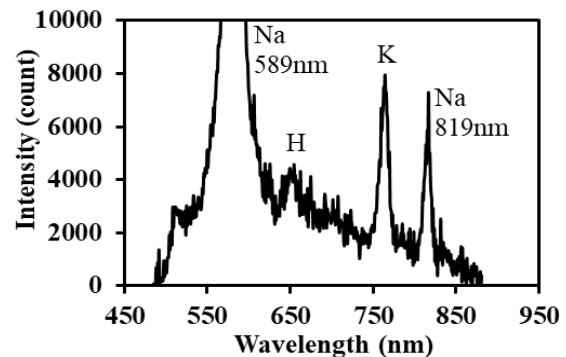
(h) Anodic pulse time 190 μs – 210 μs

Figure 5-2 The emission spectra recorded during the PEO of AZ91D Mg-alloy for different anodic pulse times.

The plasma emission was measured using an ICCD camera at an interval of 10 s during the PEO process time of 3600 s. Therefore, emission intensity was measured at 360 points throughout the process. From the measured emission spectra using ICCD camera, emission intensity at 589 nm and 819 nm was calculated by subtracting the background from the total sum of count for the specific number of data points. Figure 5-3 and Figure 5-4 show the spatial and time-resolved plasma emission intensity for Na-I line at 589 nm and 819 nm, respectively, during the PEO of AZ91D Mg-alloy for different anodic pulse times. The emission intensity results show the high-intensity peaks in the later stage of the PEO process. This high-intensity peak belongs to plasma, which is responsible for the micro-cracks and porosity in formed coating. This high-intensity peak appears after 130 µs of anodic pulse and in 1800 s of the PEO process time. Also, the measured emission spectra show emission due to collision radiative recombination after 130 µs of anodic pulse time. Therefore, controlling the anodic pulse time and the PEO process time could eliminate high-intensity plasma discharge and result in improved coating quality of AZ91D Mg-alloy. Hussein et al. [42] also concluded that coating quality could be improved by eliminating the high-intensity plasma discharges by appropriately controlling the pulse currents as well as their timing.
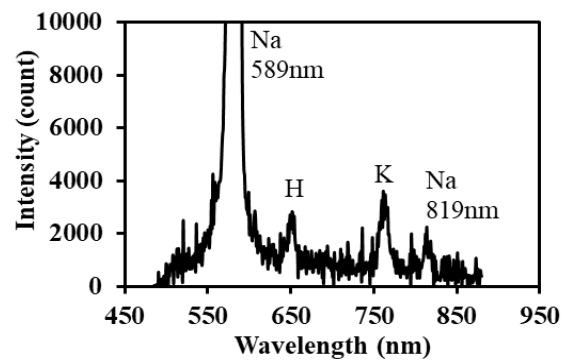
(a) Anodic pulse time 50 μs – 70 μs
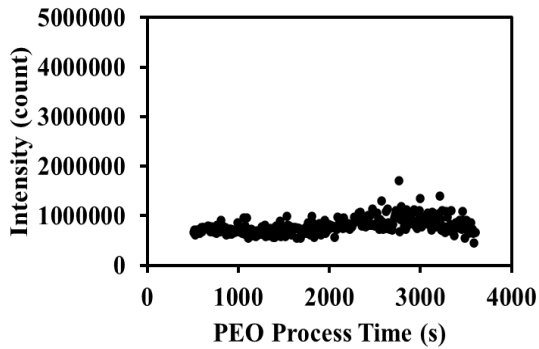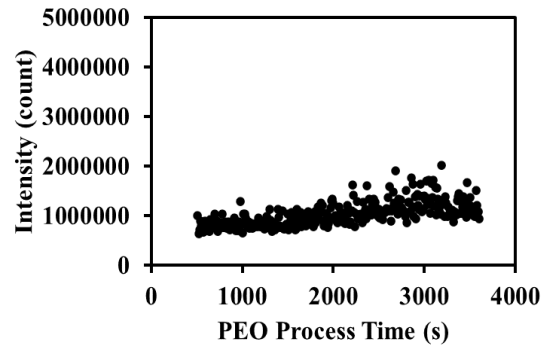
(b) Anodic pulse time 70 μs – 90 μs

(c) Anodic pulse time 90 μs – 110 μs

(d) Anodic pulse time 110 μs – 130 μs
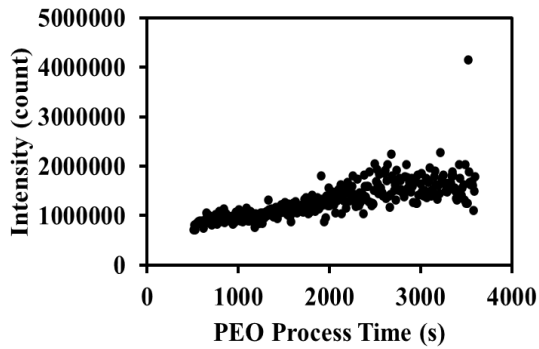
(e) Anodic pulse time 130 μs – 150 μs
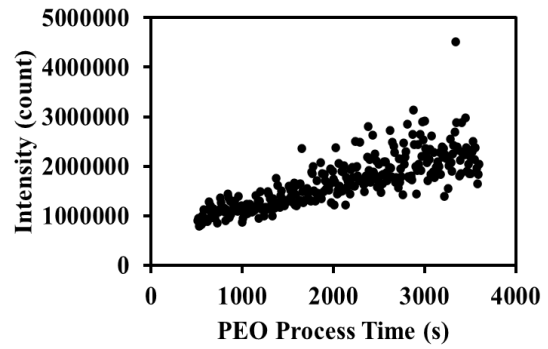
(f) Anodic pulse time 150 μs – 170 μs
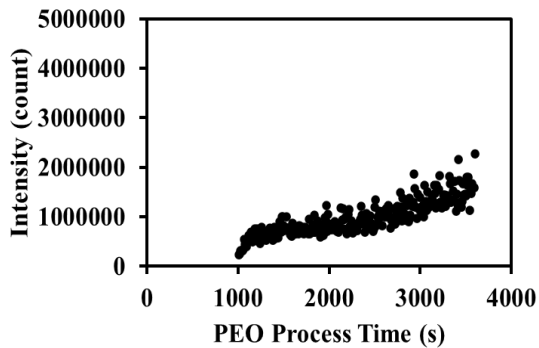
(g) Anodic pulse time 170 μs – 190 μs
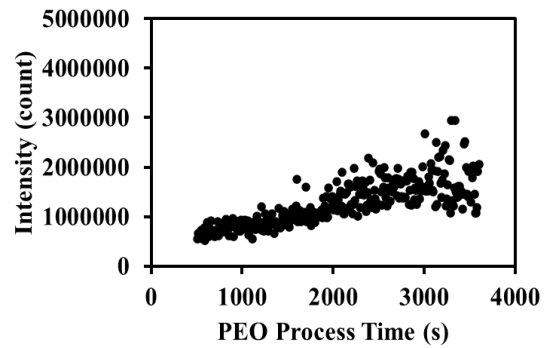
(h) Anodic pulse time 190 μs – 210 μs

Figure 5-3 The time variation of emission line intensity of Na-I at 589 nm during the PEO of AZ91D Mg-alloy for different anodic pulse times.

(a) Anodic pulse time 50 μs – 70 μs

(b) Anodic pulse time 70 μs – 90 μs

(c) Anodic pulse time 90 μs – 110 μs

(d) Anodic pulse time 110 μs – 130 μs
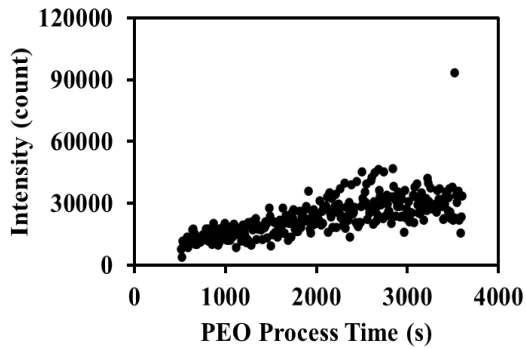
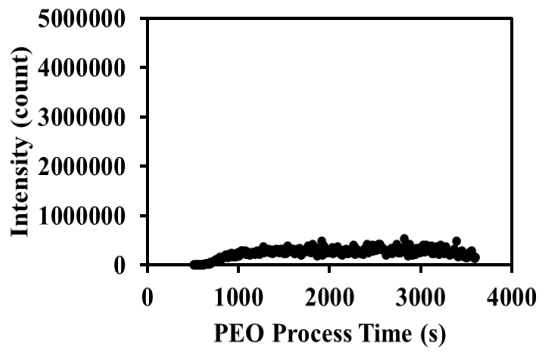(e) Anodic pulse time 130 μs – 150 μs
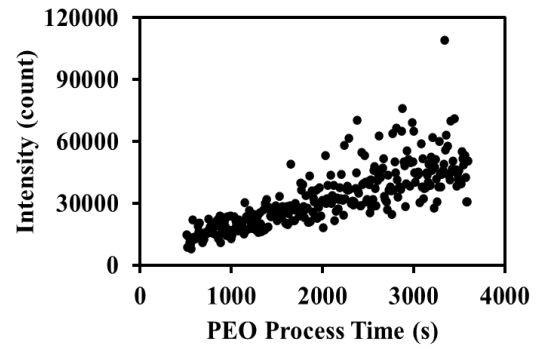
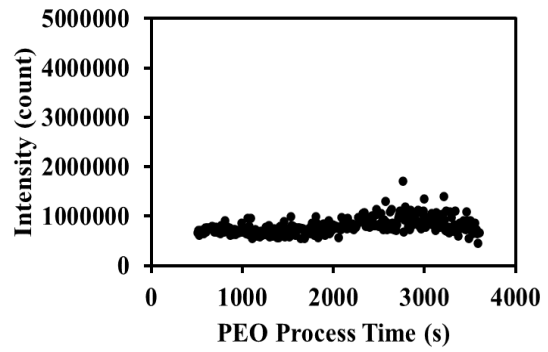(f) Anodic pulse time 150 μs – 170 μs
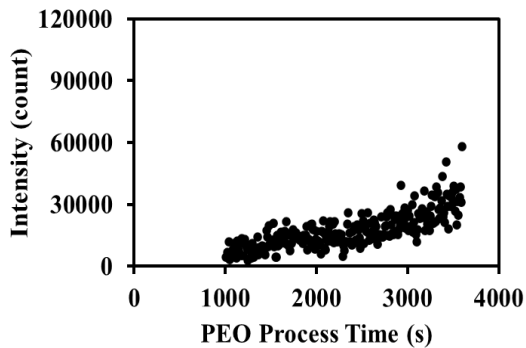
(g) Anodic pulse time 170 μs – 190 μs
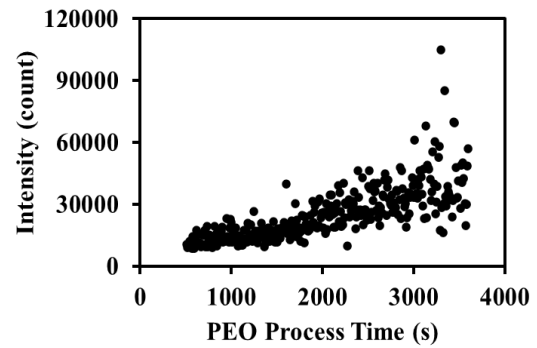
(h) Anodic pulse time 190 μs – 210 μs

Figure 5-4 The time variation of emission line intensity of Na-I at 819 nm during the PEO of AZ91D Mg-alloy for different anodic pulse times.

5.2.2 Plasma temperature

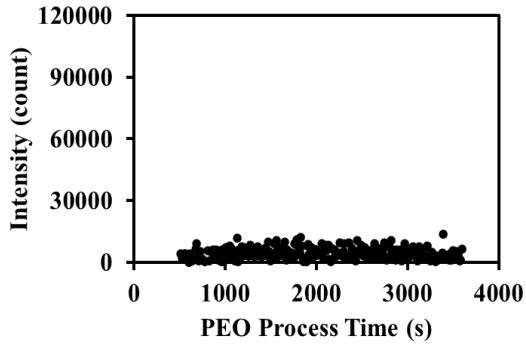The Na-I emission lines at 589 nm and 819 nm were selected to calculate the plasma temperature. Table 5-1 shows the corresponding parameters for chosen emission lines. Any spectroscopic determination of excited plasma requires the knowledge of actual light emission intensity, without self-absorption. Therefore, it is essential to consider self-absorption for Na-I emission lines. The reliability of using Na-I lines was checked by comparing the intensity ratio within multiplies with corresponding line strength ratio, see, e.g. [95], and a good agreement found. Therefore, the self-absorption test was not carried out for temperature calculation.

Table 5-1

The transition probabilities of Na-I lines [96]

Atom	Wavelength (λ) (nm)	Transition	g_k	Energy (eV)	A_{ki} (S^{-1})
Na-I	589	$2p^63s\ ^2S\ 0.5 - 2p^63p\ ^2P°\ 1.5$	4	2.104	61000000
Na-I	819	$2p^63p\ ^2P°\ 1.5 - 2p^63d\ ^2D\ 2.5$	6	3.616	54000000

The relative emission intensities of spectral lines of the same atomic species were used to calculate plasma temperature. This method is one of the classical techniques of plasma physics, and it is observed in detail in [96]. The attractive feature of this method is its simplicity because only relative line intensities have to be measured, and other atomic parameters canceled out by emission intensity ratio. Spectral lines must belong to the same atomic or ionic species. That means they must be emitted by an atom of one element in the same ionization stage. The temperature was calculated using the following expression [96].

$$\frac{I_1}{I_2} = \frac{A_{(i,j)(1)}g_{(m)(1)}\lambda_{0\ (2)}}{A_{(i,j)(2)}g_{(m)(2)}\lambda_{0\ (1)}} exp \left[\frac{E_{(m)(2)} - E_{(m)(1)}}{kT}\right] \quad (5.1)$$

Where I_1 and I_2 are relative emission line intensities of the same species; $A_{(i,j)(1)}$ and $A_{(i,j)(2)}$ are the transition probabilities of first and second emission lines, respectively. In this, i and j stand for upper and lower levels of respective lines; similarly, $g_{(m)(1)}$ and $g_{(m)(2)}$ are the statistical weight of upper levels; $\lambda_{0\ (1)}$ and $\lambda_{0\ (2)}$ are the wavelengths of lines center in a vacuum, $E_{(m)(1)}$ and $E_{(m)(2)}$ are the energies at the upper level of emission lines, and k is Boltzmann's constant; T is plasma temperature.

The plasma temperature is valid if the level populations of the lines in question are populated according to the Boltzmann law; in other words, at least LTE must exist for these levels. All quantities appear in ratios, so it suffices to use the same units for quantities corresponding to two lines in question. In particular, it is convenient to express the energies of upper levels and thermal energy in electron volts. The beauty of this method lies in its simplicity, as only relative line intensities have to be measured, a task that is usually much easier than absolute measurements of the same quantities. Also, the calculated temperature does not depend on plasma parameters, which are also of great help. On the other hand, the accuracy of the results is usually poor, because of the ratio of the line intensities is fairly intensive to the temperature at high temperatures. By differentiating equation 5.1 one readily finds that;

$$\frac{\varDelta T}{T} = \frac{kT}{\varDelta E}\frac{\varDelta R}{R} \quad (5.2)$$

$$\Delta E = E_{m(1)} - E_{m(2)} \quad (5.3)$$

$$R = \frac{I_1}{I_2} \quad (5.4)$$

If $kT/\varDelta E$ is greater than or equal to 1, the error in the relative line intensities is magnified, resulting in significant inaccuracies of temperature. [96] However, if $kT/\varDelta E$ is smaller than 1, as in the case of our study, temperature accuracy is acceptable.

As discussed in section 2.2, the emitted light can be absorbed by the electrolyte solution. Therefore, before temperature calculation, emission intensity at 589 nm and 819 nm was calibrated using the transmittance of an electrolyte solution at the respective wavelength. Figure 5-5 shows the time variation for transmittance of an electrolyte solution at 589 nm and 819 nm. The measurement was repeated five times, and the average of five measurements was considered as transmittance at the respective wavelength. The temperature was calculated at 360 measurement points during the processing time of 3600 s. The trendline was used to calculate transmission at each temperature calculation point. The transmittance at 1800 s was disturbed because oxide precipitate in solution attracted towards sample during the PEO process. The solution becomes apparent when oxide in it depletes due to coating formation. The emission intensity of Na-I lines at 589 nm and 819 nm also calibrated by a system calibration factor. The measurement system was calibrated, as explained in section 2.1.
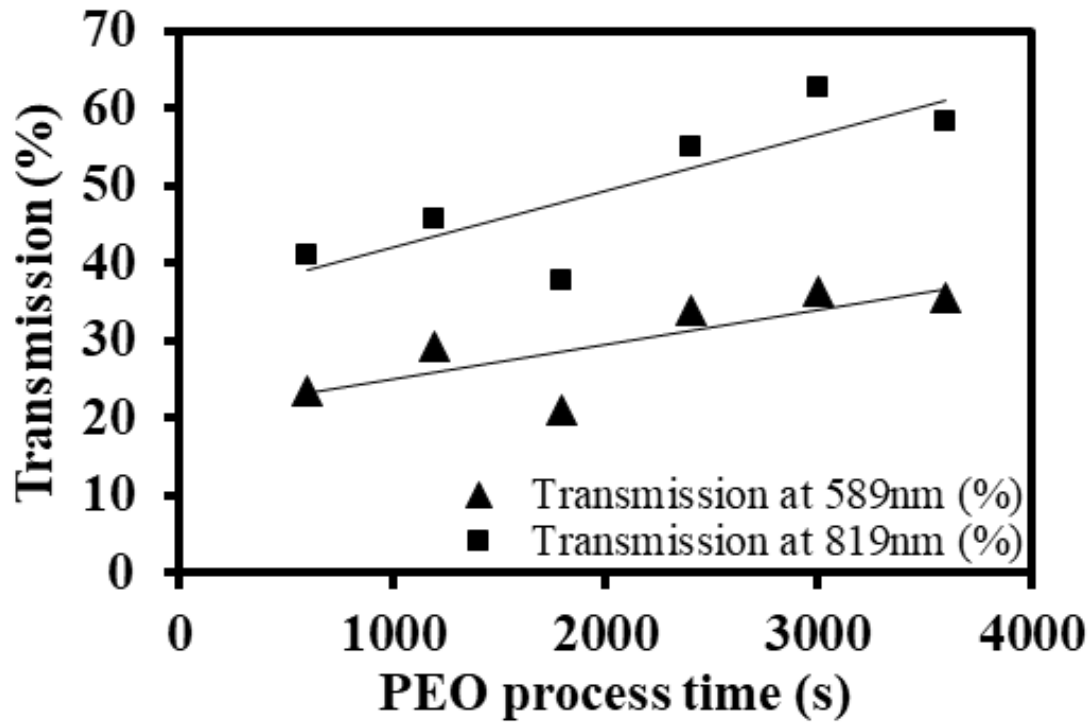
Figure 5-5 The time variation of solution transmission at 589 nm and 819 nm during the PEO of AZ91D Mg-alloy.
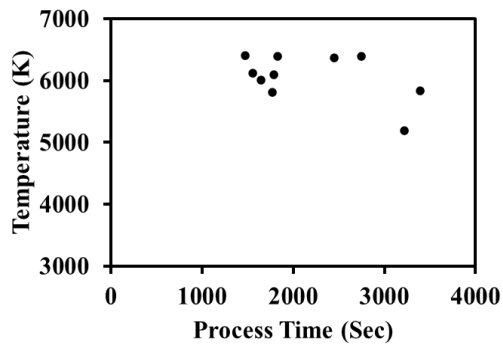
(a) Anodic pulse time 50 μs – 70 μs
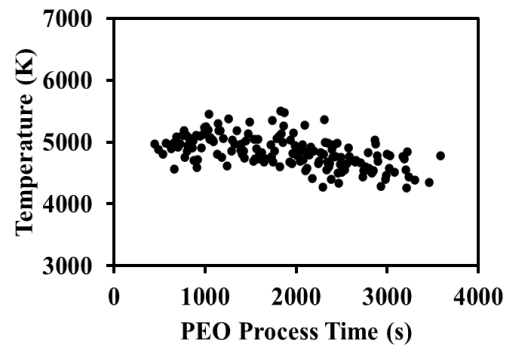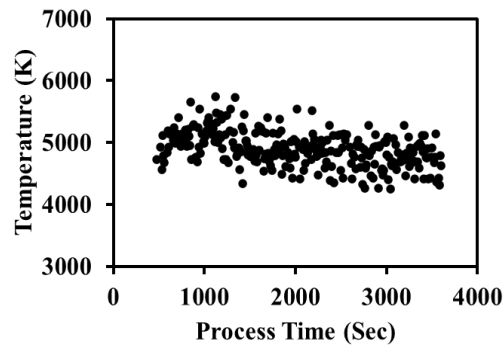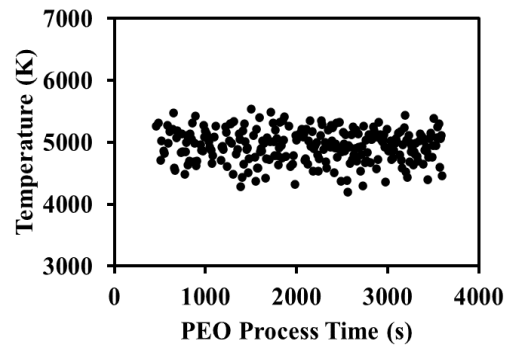
(b) Anodic pulse time 70 μs – 90 μs

(c) Anodic pulse time 90 μs – 110 μs

(d) Anodic pulse time 110 μs – 130 μs
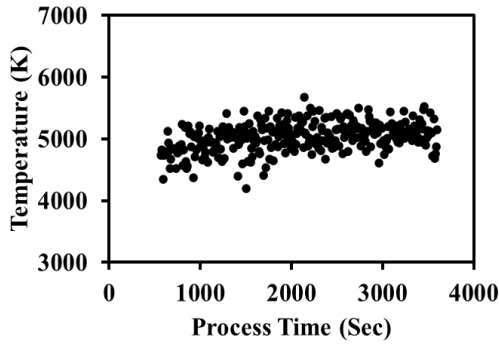
(e) Anodic pulse time 130 μs – 150 μs　　　(f) Anodic pulse time 150 μs – 170 μs
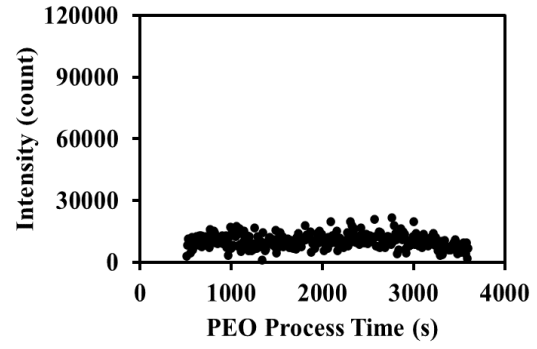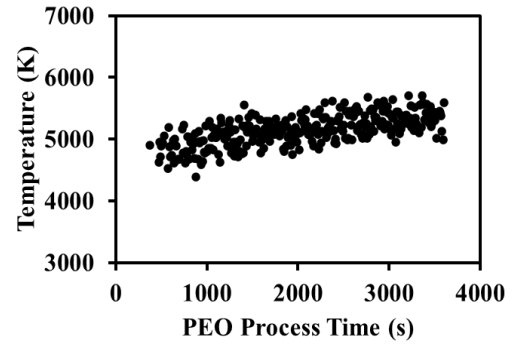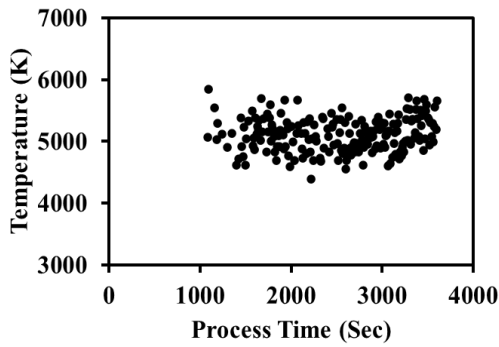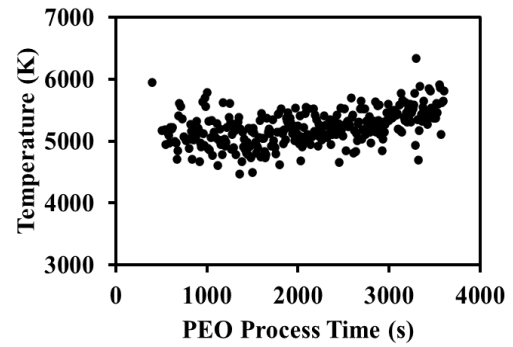

(g) Anodic pulse time 170 μs – 190 μs　　　(h) Anodic pulse time 190 μs – 210 μs
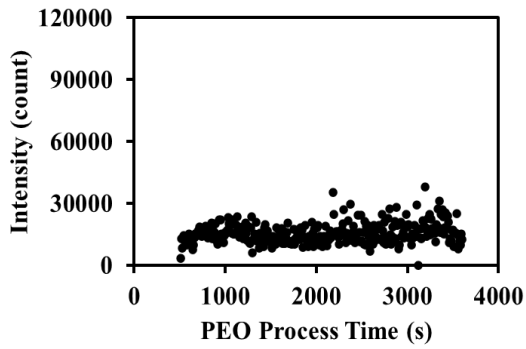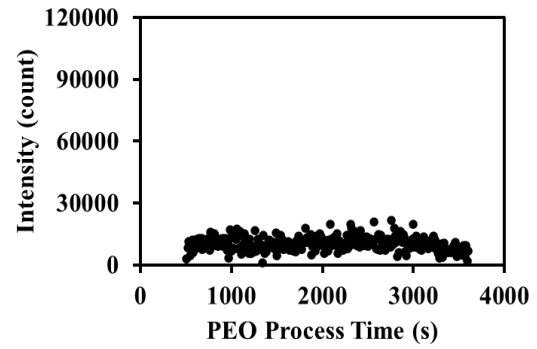
(i)

Figure 5-6 The plasma temperature as a function of the PEO process time (s) determined from the intensity ratio of Na-I (589 nm) / Na-I (819 nm) for different anodic pulse times.

It is universally accepted that discharge in PEO occurs when applied voltage reaches a critical value (breakdown voltage) for the oxide layer. This was responsible for plasma discharge formation and intense light emission generated at various sites of the sample surface. Figure 5-6 shows the variation of calculated plasma temperature for different scanning times throughout the PEO process. The temperature in the spark discharge zone was found in the range of 4200 K to 6400 K, which is in good agreement with previous results for Mg-AJ62 alloy [42]. The plasma temperature for anodic pulse time 50 μs – 70 μs shows temperature only at 10 points out of 360. This is because of the weak emission intensity of Na-I line at 819 nm at the beginning of anodic pulse time. From measured results, for anodic pulse time, 70 μs – 90 μs, and 110 μs – 130 μs, a ratio of maximum to minimum emission intensity from 500 s to 3600 s of process time was three for both. However, for 70 μs – 90 μs, plasma temperature decreases from a maximum of 5503 K ± 238 K to a minimum of 4265 K ± 121 K and for 110 μs – 130 μs, plasma temperature shows the constant trend with variation in between 4193 K ± 129 K to 5543 K ± 252 K. For anodic pulse time of 150 μs – 170 μs and 190 μs – 210 μs, a ratio of

maximum to minimum emission intensity from 500 s to 3600 s of process time was five for both. However, plasma temperature increases from 4393 K ± 180 K to 5708 K ± 205 K and 4472 K ± 172 K to 6336 K ± 254 K respectively. However, for the case of 70 μs – 90 μs, it was found that plasma temperature decreases with an increase in processing time. It might be because of the delayed dissolution of t-ZrO_2, $Mg_2Zr_5O_{12}$, and MgO phases in the electrolyte solution in a later stage of the process. In PEO, the dissolution of previously formed coating and formation of the new coating co-occurs [97]. In this study, the electrolyte solution with pH 11.6 was used, and the ceramic coating was mainly composed of t-ZrO_2, $Mg_2Zr_5O_{12}$, and MgO phases [70, 98]. These phases are difficult to dissolve in electrolyte [99]. The dissolution of the outer layer significantly reduces, while the magnesium sample oxidized. Therefore, strong plasma discharge emission is found in the later stage.

It is essential to note that temperature results reported in [99, 100] are different from our temperature results. It is mainly because of different working conditions during the PEO process. For example, applied modes of power supply, sample material, electrolyte solution, and other parameters. Hussein et al. [42] studied the effect of current mode on plasma temperature during the PEO coating on Mg-AJ62 alloy and found that compared to the unipolar current process, the application of pulsed bipolar current resulted in reducing the high spikes on temperature profiles and the average plasma temperature. They also concluded that it is possible to eliminate the high-intensity plasma discharges and high-temperature spikes by appropriately controlling the ratio of positive to negative pulse currents as well as their timing. Therefore, the quality of coatings could improve. From the measured emission spectra, it was found that emission due to collision radiative recombination appears after 130 μs of anodic pulse time. Also, measured emission intensity using ICCD camera and photodetector shows the same behavior. Emission intensity was stable until 130 μs of anodic pulse time and 1800 s of the PEO process time. Controlling these timings could eliminate high-intensity plasma discharge and result in improved coating quality of AZ91D Mg-alloy. Thus, spatial and time resolved plasma emission measurement approach successfully evaluate processing parameters to control the PEO process.

Chapter 6

Experimental results and discussion III: Discharge model

An understanding of the discharge processes is very helpful in clarifying the mechanisms of the PEO process. It is worth mentioning that the high-intensity peaks during the later stage of the anodic pulse shown in Figures 5-3 and Figure 5-4 indicate the appearance of strong discharges during the process. Therefore, the plasma discharge model is discussed in this chapter.

6.1 Voltage Behavior

Figures 6-1 shows the typical output anodic voltage response concerning process time. The result shows a sharp increase in voltage at the beginning of the process. It mainly involves the rapid electrochemical formation of the initial insulating oxide film. The breakdown voltage was not reached yet. For the anodic pulse time, 70 µs – 90 µs, 90 µs – 110 µs, 110 µs – 130 µs, 130 µs – 150 µs, 150 µs – 170 µs and 190 µs – 210 µs, the rate of voltage increase for the first 120 s was higher than 1.3 V s^{-1}. During this time, plasma density was rather high and decrease with an increase in reaction time. It indicates that there was a quick dissolution rate of alloying elements at the start of the reaction. [101] However, it reduces with a reduction in the rate of voltage increase to less than 166 mV s^{-1} from 180 s to 420 s. The rate of voltage increase reduces to less than or equal to 33 mV s^{-1} from 540 s to end of the process. However, for the anodic pulse time, 50 µs – 70 µs and 170 µs – 190 µs, constant voltage increase was delayed and hence the plasma appearance was delayed. This may happen because of delayed electrochemical formation of the initial insulating oxide film, which keeps the resistance high enough and voltage below the critical breakdown voltage.
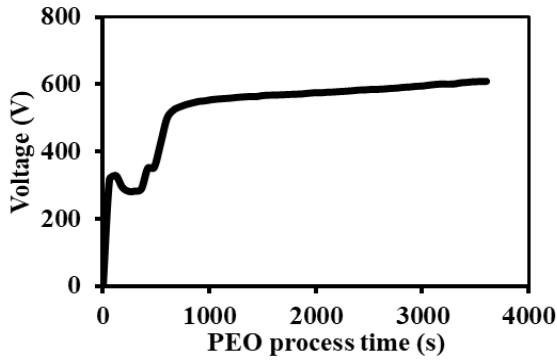
(a) Anodic pulse time 50 μs – 70 μs
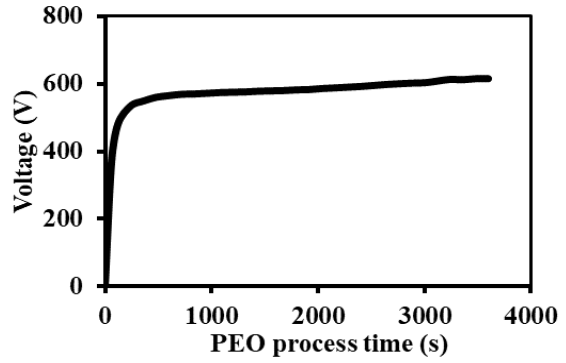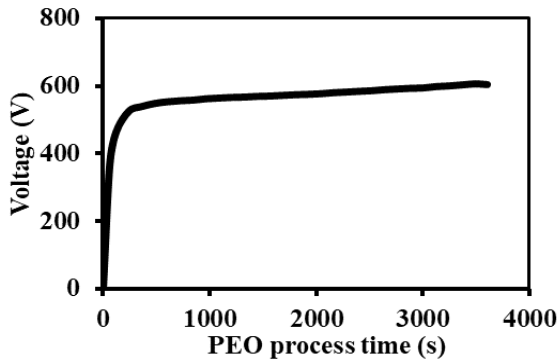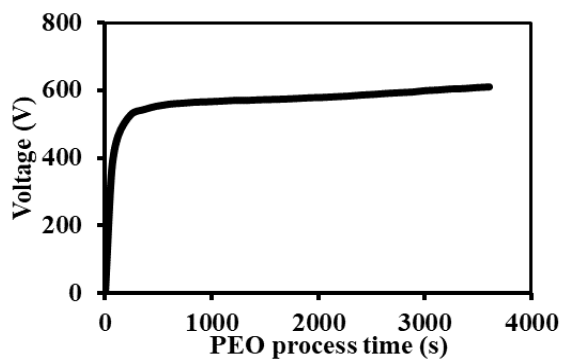
(b) Anodic pulse time 70 μs – 90 μs

(c) Anodic pulse time 90 μs – 110 μs

(d) Anodic pulse time 110 μs – 130 μs
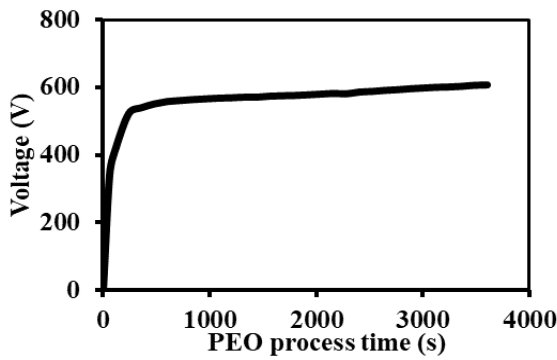
(e) Anodic pulse time 130 μs – 150 μs
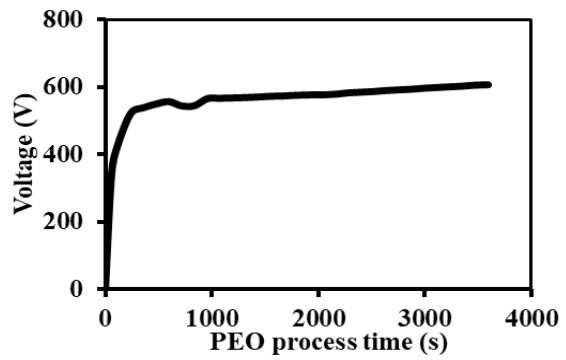
(f) Anodic pulse time 150 μs – 170 μs
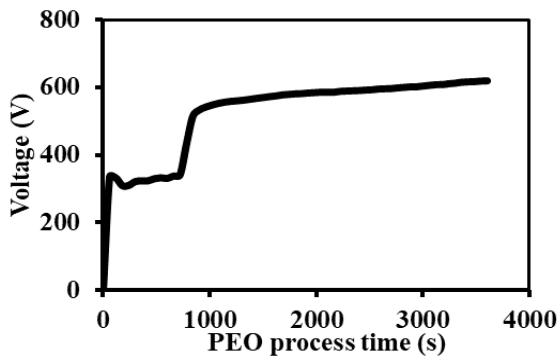
(g) Anodic pulse time 170 μs – 190 μs
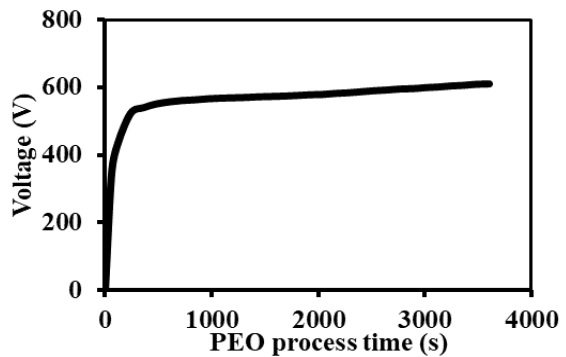
(h) Anodic pulse time 190 μs – 210 μs

Figures 6-1 The typical anodic voltage response during the PEO of AZ91D Mg-alloy for different anodic pulse times.

6.2 Plasma discharging appearance

As the plasma coating process proceeds, the discharge appearance changes, and the plasma emission intensities varied, as shown in Figures 5-3 and Figure 5-4. These plasma discharge appearances can be summarized for the four stages as follows:

Stage I: In this stage where the breakdown voltage is not yet reached, no OES signal could be detected.

Stage II: This stage is characterized by numerous sparks moving rapidly over the whole sample surface area. There is a significant increase in the plasma emission intensity at the beginning of stage II. It then continues to increase with the anodic pulse time and the PEO process time. This indicates a start of the oxide layer breakdown, an increase in temperature; therefore, the melting of the sample metal, as can be seen from the electron temperature results in Figure 5-6. The higher temperature will be sufficient to excite the atoms, and hence the de-excitation radiation signal can be detected. From the plasma images in Figure 4-2 (c) and (d), it is easy to distinguish this stage, the presence of small signals indicates the beginning of the spark without seeing any noticeable increase in the intensity at the beginning of this stage. It is probably due to low current density, which is not sufficient to excite a large number of atoms. The temperature results in Figure 5-6 do not show the temperature plot before 600 s of the PEO process time. This is because of weak Na-I line emission in this stage. The transition between stages II and III is characterized by a low variation in the emission intensity signal, as shown in Figures 4-2, 5-3, and 5-4.

Stage III: This stage was characterized by a larger but slower moving discharge. As the oxide layer grows, its electrical resistance increases, therefore the nature of the plasma changed as was seen from the emission intensity signals. This stage showed variations in the intensities in terms of being a strong appearing group of peaks, indicating strong discharges. One of the main points of interest in these signals is their consistency with the signal from the species in terms of general shape and timing, as shown in Figures 4-2, 5-3, and 5-4. These signals may be interpreted as: at these concentrated local discharges, the local plasma temperature is high enough to excite all the species that exist in those locations at that particular time. The low intensity and temperature variation, which appeared at the end of stage III, were followed up by the appearance of strong but largely separated signals. That indicates the beginning of stage IV of the process.

Stage IV: At this stage, concentrated discharges appear as relatively large and long-lasting sparks. Large separations were also seen between these strong groups of signals. The strong signals resulted from the long-lasting, strong discharges which create more than sufficient energy to cause such intensive ionization processes. However, from the plasma images in Figures 4-2, the occurrence of the strong discharges is less frequent than that in stage III due to the thicker coating causing more difficulty in the initiation of such discharges. In some cases, such strong discharges may cause irreversible damage to the coatings in this stage.

6.3 Interpretation of the plasma discharge model

An important consequence of the occurrence of surface discharges is the development of metallurgical processes in the growing of the oxide layer, which are induced by the heat liberated in discharge channels from electron avalanches. This instantaneous local heating leads to melting, quenching, and recrystallization of the substances deposited onto the surface. The direction and intensity of the deposition processes depend on the density and power of discharges, which are a function of the coated thickness. Several micro discharge formation models have been proposed [102-106].

In earlier work [75], three individual models of discharge formation in the PEO process were suggested. The first model defined the micro discharge's appearance as a result of oxide film dielectric breakdown in a strong electric field, the second one considered each discharge as a gas discharge occurring in a micropore of the oxide film (believed to be induced by an initial dielectric breakdown of a barrier layer in the bottom of the micropore [75]), and the third model assumed the possibility of free electron generation and glow discharge ignition in the gaseous media at the oxide-electrolyte interface, which leads to heating, melting and quenching the underlying oxide layer.

Hussein et al. [100] proposed a model with three types of discharges as metal-oxide interface discharge, oxide-electrolyte interface discharge within the upper layer of coating, and discharge at the top layer of coating. In their discharge model, only metal-oxide interface discharge was considered to have a discharge channel from the metal-oxide interface to the coating surface. However, we believe that every plasma should have a discharge channel which carries the current from metal-oxide interface to the coating surface. Therefore, there is not enough evidence to support the assumption of discharge type generating within the upper layer of

coating, as suggested in Ref. [100]. The glow discharge in gas media occurs at an oxide-electrolyte interface, which finally induces the dielectric breakdown of the oxide coating. Refs. [75, 107] also gives evidence of the dielectric breakdown of PEO coating, and every spark corresponds to the discharge channel through a metal-oxide interface. Therefore, plasma discharge emission was distinguished into two categories: one, discharge emission due to the oxide layer breakdown at the surface due to a strong electric field. Second, plasma discharges at the metal-oxide interface, which corresponds to small and high-intensity discharge depending on the discharge channel.

Figure 6-2 shows a schematic illustration of the model describing the appearance of plasma discharge during different anodic pulse time and PEO process time. When voltage increases to a critical value, the breakdown of oxide coating occurs with the formation of spark discharge. Therefore, one type of production of the signals from discharge emission due to the oxide layer breakdown at the surface due to a strong electric field, which is a type A in Figure 6-2. During the PEO process, when the electric field strength in the oxide layer reaches a critical value beyond which the film breaks down, a localized melt channel is formed, and plasma reactions take place in these channels. Then there is a consistency of the signals from all species existing in the plasma. The radiation intensities of the species are related to excitation caused by electron impact under a high electric field imposed on the discharge channel. Because of the high temperature and the strong electric field, molten metal is ejected from the metal-oxide interface into the oxide coating surface, where it is rapidly solidified by the electrolyte. Therefore. The second type of production of the signals from discharge emission due to spark at the metal-oxide interface through the discharge channel (micropores) of the formed oxide coating. At the beginning of the PEO process, thin oxide coating is easy to breakdown; therefore, small size plasma discharge appears. As the coating layer thickens with time, the breakdown voltage of the coating becomes high. Therefore, plasma discharge emission increases respectively, which is believed to depend on the size of the discharge channel. Therefore, from the measured emission intensity and plasma temperature results, the second type of plasma emission divided into three categories as type B1, B2, B3 in Figure 6-2, depending on plasma emission intensity. The spatial resolved and time resolved plasma emission measurement approach allows us to predict the appearance of the plasma discharge type according to the anodic pulse time and the PEO process time.
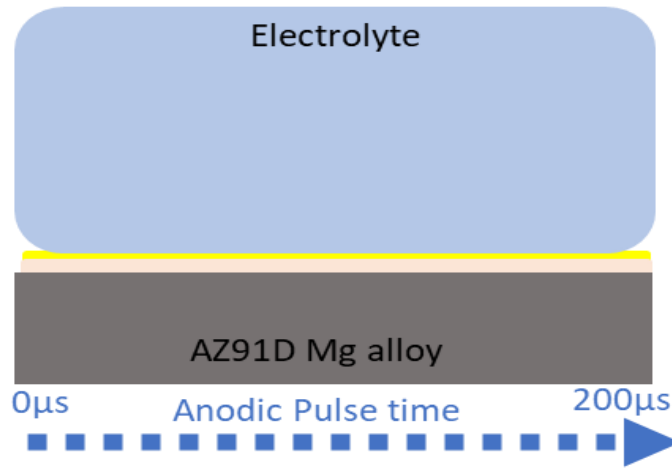
(a) The PEO process time - initial
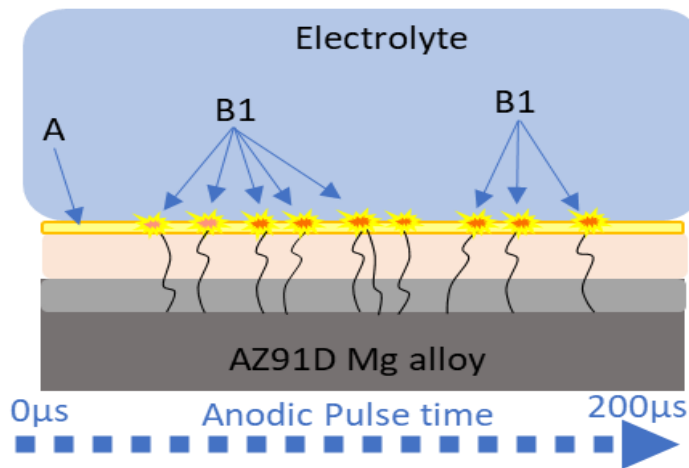
(b) The PEO process time - around 900 s
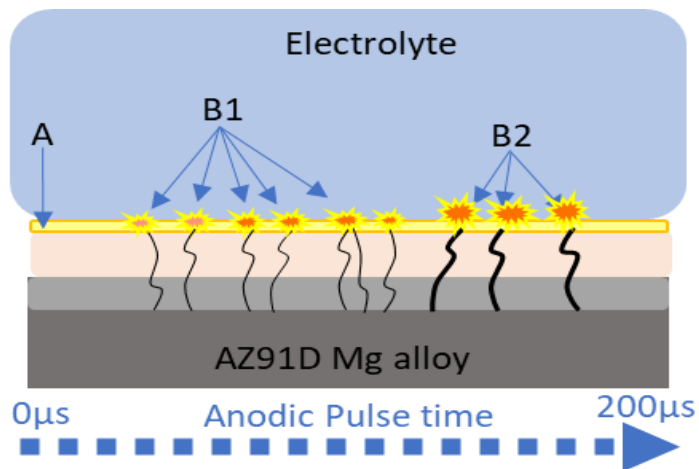
(c) The PEO process time - around 1800 s
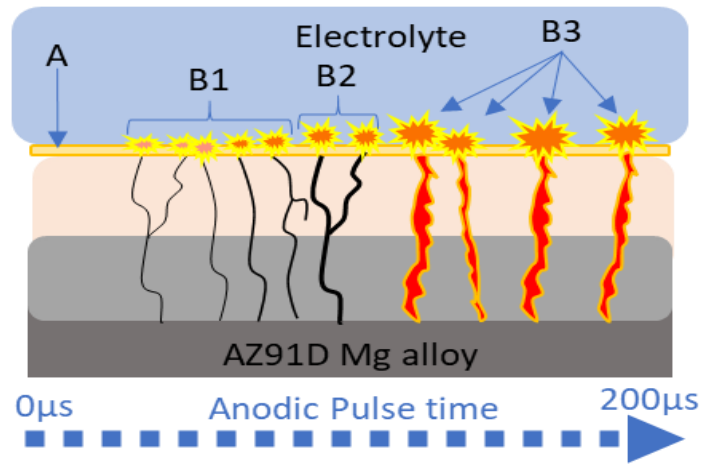
(d) The PEO process time - around 2700 s to end of the process

Figure 6-2 Schematic illustration of the model describing the appearance of plasma discharge according to the anodic pulse time and processing time of the PEO process.

Chapter 7

Experimental results and discussion IV: Effect of current density on plasma emission

Considering the challenges of development and controlling the PEO process, many researchers introduced special current regimes such as bipolar current pulse. [108-111] The arcing during the PEO process in a later stage is responsible for the micro-cracks or micro holes in the coating and hence the porous nature of the coating. The anodic to cathodic current ratio is an important parameter to reduce arcing that usually causes defects in the oxide layer. [74, 101] The soft sparking regime can be included in the conventional PEO regime to achieve a thick, dense, and homogeneous layer. But, plasma emission behavior concerning time was not reported yet. Therefore, bipolar pulse constant current mode with different current ratios was applied to a sample. The effect of the current ratio on plasma emission behavior was studied during the PEO process. Case 9 and case 10 in Table 4-1 shows the processing parameters considered for this study. The plasma emission was monitored as a function of anodic pulse throughout the PEO process using photodetector and ICCD camera. For the emission measurement using a photodetector, the optical arrangement is shown in Figure 3-4 (b) was used, and for the case of OES measurement by ICCD camera, the optical arrangement is shown in Figure 3-4 (a) was used. The plasma image was also recorded during the PEO process.

7.1 Voltage behavior

Figure 7-1 shows the typical output anodic voltage change during the PEO process for case 9 and case 10. The voltages show the linear increase at the beginning with weak emission intensity, and then the voltages increase evenly with plasma emission in case 9 and case 10. However, in case 9, the voltage decreases rapidly after 786 s. The phenomena can be observed according to the plasma images of the PEO process according to time, as illustrated in Figure 7-2. The plasma quenched very rapidly from 786 s to 788 s, and the plasma emission became very weak after the 840 s. These images show the change of plasma emission from arc regime to soft regime. The results indicate that the soft regime was included when the current ratio was less than 1 for case 9, which reduces the plasma emission. It is necessary to understand the plasma emission behavior during arc regime and soft regime with time. Therefore, the plasma emission was detected by photodetector and ICCD camera in the PEO process.
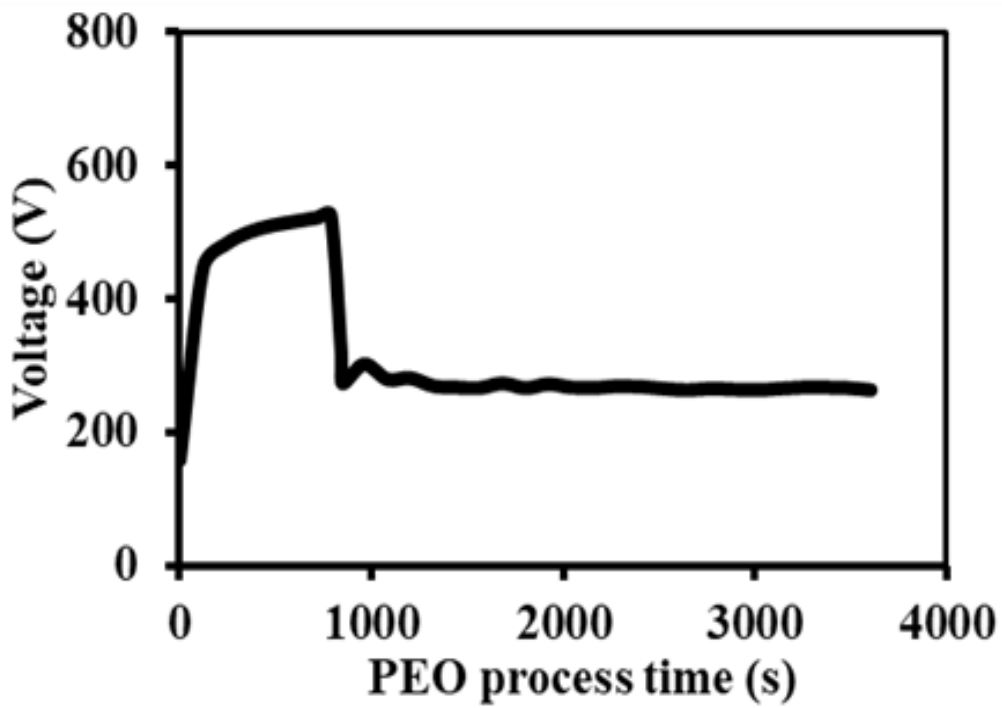
(a) Case 9
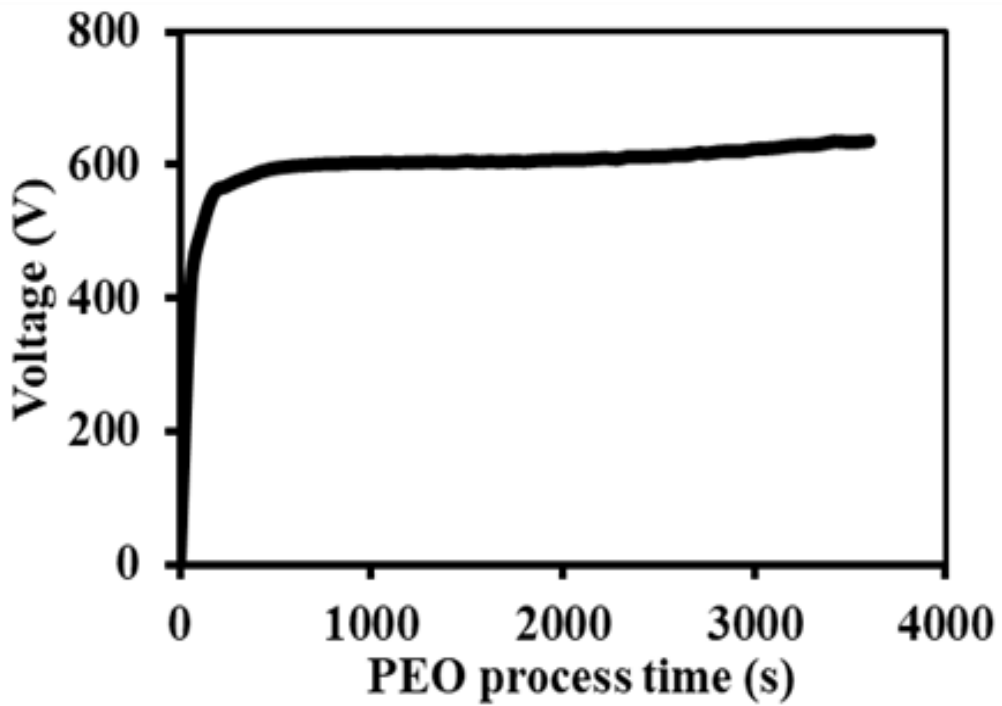
(b) Case 10

Figure 7-1 The typical anodic voltage response for case 9 and case 10 of table 4-1 during the
PEO of AZ91D Mg-alloy.

(a) 781 s

(b) 782 s

(c) 783 s

(d) 784 s

(e) 785 s

(f) 786 s

(g) 787 s

(h) 788 s

(i) 840 s

(j) 960 s
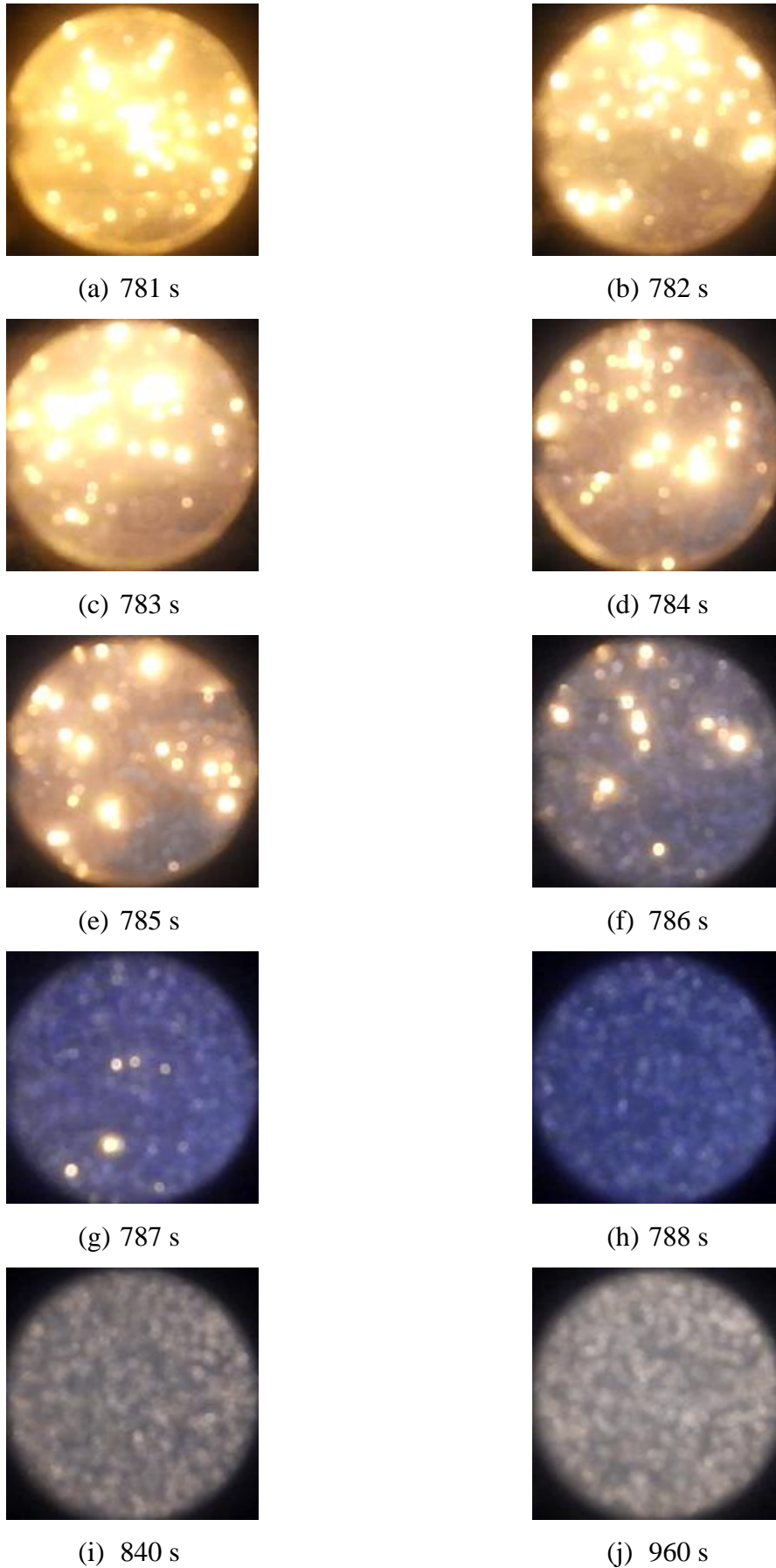
Figure 7-2 The Plasma images by a camera in case II from arc regime to soft regime.

7.2 Emission measurement using a photodetector

Figure 7-3 shows the anodic voltage pulse along with simultaneously measured plasma emission signal by a photodetector, which shows that plasma emission from the discharge sample correlates with an applied bipolar current pulse. It was found that discharge behavior changes according to the change of the current ratio. For case 10 in Figure 7-3 (b), the emission intensity increases with increasing the anodic pulse time. However, case 9 in Figure 7-3 (a) shows different emission behavior during arc and soft regimes. Arc regime in case 9 shows 14 µs delay in the PEO process of 900 s. The emission intensity also increases rapidly first and then reduces and becomes constant. In a soft regime, the emission intensity is very weak, which increases with raising voltage and reduces gradually with an increase in anodic pulse time. Therefore, the PEO process can be controlled by the current ratio.
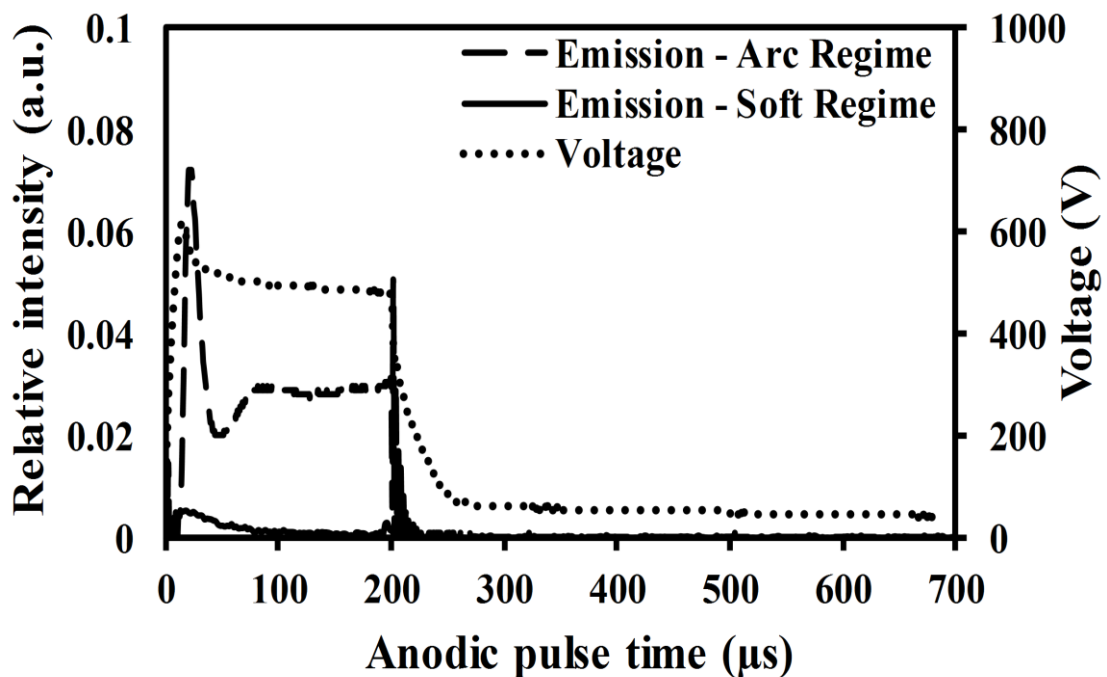
(a) Case 9
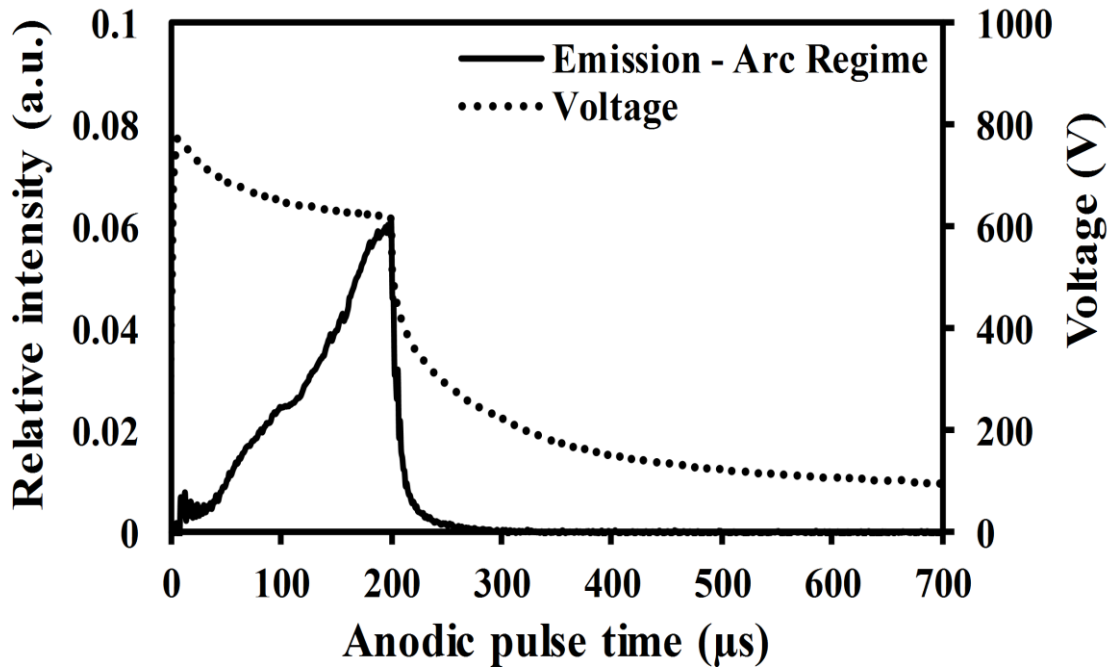
(b) Case 10

Figure 7-3 The measured plasma emission behavior using photodetector in different cases during the PEO of AZ91D Mg-alloy.

7.3 Emission measurement using the ICCD camera

The plasma emission was also detected by the ICCD camera. Figure 7-4 shows the measured spectra of case 9 in arc regime and soft regime during the PEO process. In arc regime, the measured spectra show the atomic emission lines of Na at 589 nm and 819 nm, H at 656 nm, which are from the electrolyte solution. The background of measured spectra is non-uniform resulted from bremsstrahlung radiation of electrons and collision radiative recombination [92-93]. However, only continuous spectra are observed in the soft regime in Figure 7-4. But plasma images and emission measured by the photodetector in Figure 7-2 and Figure 7-3 shows emission intensity. Therefore, emission in a soft regime was measured for a large number of cycles. Figure 7-5 shows the measured emission spectra in a soft regime at 840 s for 10 accumulations and 350 accumulations. These results prove that there is no obvious atomic or ionic excitation in a soft regime. The observed emission in the soft regime was created by charged free particles because of free radiation. According to the measurement results of plasma emission in different cases, the soft regime presents the improved performance for protective oxide coating.

55
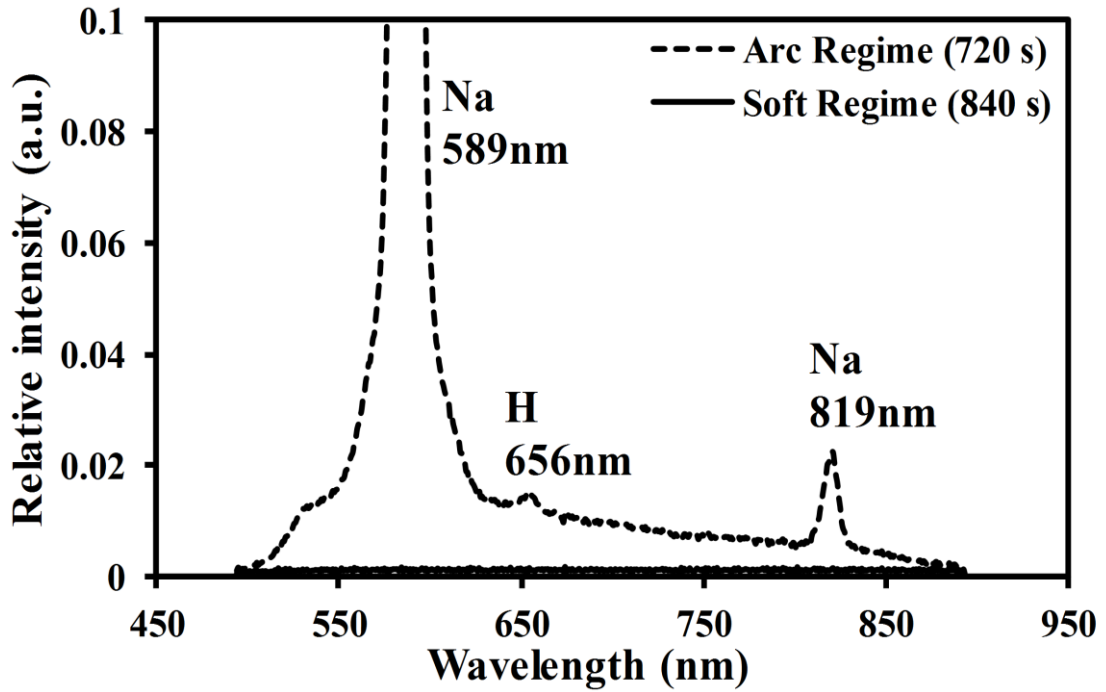
Figure 7-4 The measured plasma emission spectra using the ICCD camera for arc regime and soft regime during the PEO of AZ91D Mg-alloy.
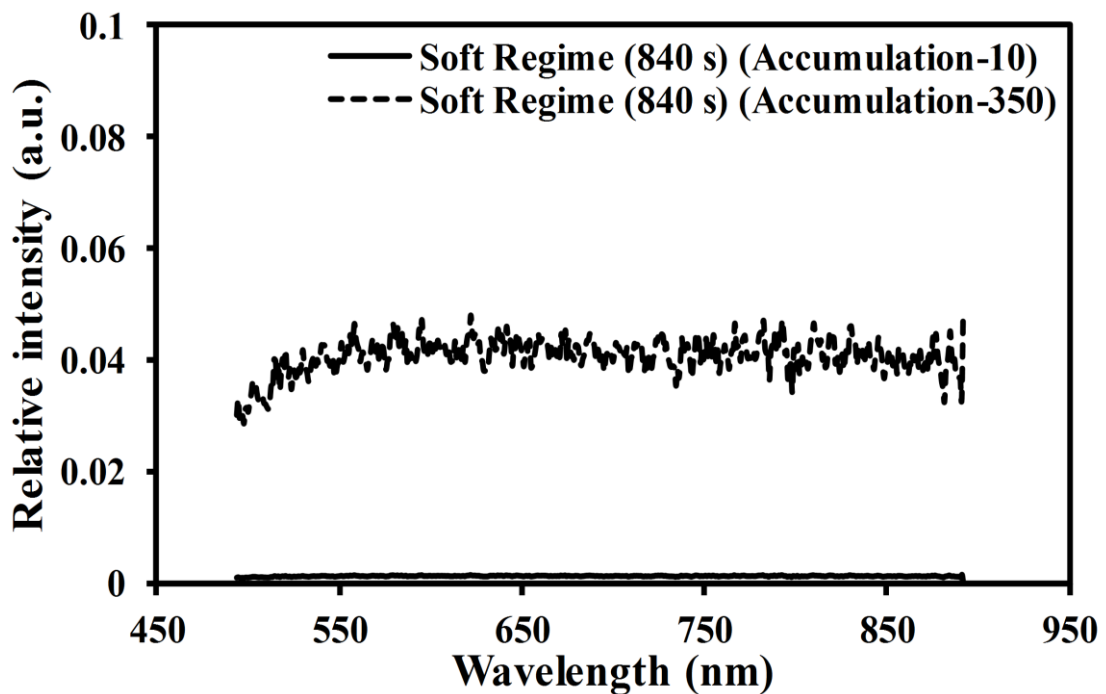
Figure 7-5 The measured plasma emission spectra using an ICCD camera in a soft regime at different accumulation during the PEO of AZ91D Mg-alloy.

Chapter 8
Summary and Conclusion

8.1 Summary

The PEO is an effective method to provide protection coating for Mg and its alloys. Meanwhile, the advantages and shortcomings of this technique are also quite obvious. Since the corrosion resistance of Mg is always the priority in practical applications, its corrosion protection by PEO coatings is of particular interest. Considering recent developments in PEO coatings on magnesium and its alloys, with various methods emerging to form an impermeable coating above chapters, explains methods for evaluation of the PEO process parameters on Mg-alloy and to control the process. Following is the summary of each chapter;

Chapter 1 introduce the background with the aim and objective of this research study. Chapter 2 introduced the general principle and characteristics of the PEO process with the formation mechanism of coating on magnesium and its alloys. Microstructure and phase composition of the PEO coatings on Mg-alloys are also discussed with recent developments and challenges in this research area. This chapter also introduces plasma spectroscopy. Chapter 3 briefly introduced the experimental methods and optical arrangements used in this work using measurement devices as the ICCD camera and a photodetector. The application of these measurement methods enables a comprehensive understanding of the plasma emission behavior during the PEO process. It also provides an effective means to fulfill the objectives mentioned in Chapter 1. Detailed information on the application of these methods is provided and discussed in the following chapters. Chapter 4 briefly introduced the reason for choosing the input electrical parameters and bipolar pulse time to study spatially resolved and time resolved plasma emission with time. The special resolution for emission measurement was evaluated from the plasma image collected by a video camera. Further, time resolution for emission measurement was evaluated using the spatially resolved emission measurement during the anodic pulse using a photodetector. From the measured results, it was decided to measure the emission intensity from the spatial resolution of 0.25 mm^2 and a time resolution of 20 µs for OES measurement using the ICCD camera.

Chapter 5 introduced the plasma emission behavior concerning an anodic pulse time and the PEO processing time. First, plasma emission was measured with anodic pulse time using a photodetector. From the measured emission intensity, it was found that emission intensity was

stable until 130 μs of anodic pulse time and 1800 s of the PEO process time. Second, the plasma emission was monitored using an ICCD camera and found that emission due to collision radiative recombination appears after 130 μs of anodic pulse time. Also, plasma temperature shows an increasing trend after 130 μs of anodic pulse time. Therefore, it can be said that high-intensity plasma, which is responsible for micro-cracks and micro holes in formed coating, appears after anodic pulse 130 μs and processing time of 1800 s. Controlling these timings could eliminate high-intensity plasma discharge and result in improved coating quality of AZ91D Mg-alloy. Chapter 6 introduced the anodic output voltage concerning the PEO processing time with plasma discharging appearance theory. Depending on the applied anodic voltage behavior, discharge appearance was divided into four stages; first, the breakdown voltage is not yet reached, and no discharge appears during this stage. Second, it indicates the start of the breakdown of the oxide layer and starts the discharge appearance. The transition between stages II and III is characterized by a low variation in the emission intensity signal with a larger but slower moving discharge. In stage four, concentrated discharges appear as relatively large and long-lasting sparks. Large separations were also seen between these strong groups of signals. Based on the measured results in this study, it is believed that every plasma should have a discharge channel which carries the current from metal-oxide interface to the coating surface. Based on it, plasma discharge emission was distinguished into two categories: one, discharge emission due to the oxide layer breakdown at the surface due to a strong electric field. Second, plasma discharges at the metal-oxide interface, which corresponds to small and high-intensity discharge depending on the discharge channel. Chapter 7 introduced the effect of applied current density on plasma emission behavior with time during the PEO process. It was found that a soft regime can be introduced during the PEO process by controlling the applied current density. For the case of applied anodic to cathodic current ratio less than 1, sudden voltage drop appears after some time from the start of the process. The plasma quenched very rapidly after the voltage drop and soft regime starts. From the emission results measured using a photodetector, it was found that the emission intensity in the arc regime increases rapidly first and then reduces and becomes constant. However, in a soft regime, the emission intensity is very weak, which increases with raising voltage and reduces gradually with an increase in anodic pulse time. From the measured OES results using the ICCD camera, it was found that there is no obvious atomic or ionic excitation in a soft regime. The observed emission in the soft regime was created by charged free particles because of free radiation.

8.2 Conclusion

Plasma Electrolytic Oxidation (PEO) is a promising technique to form the protective oxide coating for the light metals and its alloys. The bipolar pulse constant current mode with 500 Hz frequency and 10% duty ratio at different current ratios and different pulse timing was applied to an AZ91D Mg-alloy sample to study the plasma emission behavior concerning time. The change in the ON / OFF timing of applied bipolar pulse current leads to a change in plasma stability and variation in output anodic voltage. The change in the applied current ratio (anodic to cathodic) at the same frequency and duty ratio effect on the appearance of plasma spark during the PEO process. The current ratio of greater than one shows only arc regime with the continuous increase in emission intensity and voltage throughout the PEO process. In contrast, the current ratio of less than one initially shows an arc regime with a gradual increase in the plasma emission and voltage and later shows a soft regime with a sudden drop in the plasma emission intensity with voltage.

The measurement and analysis of visible and near UV wavelength emissions from plasma using OES provide a valuable diagnostic tool for the study of the PEO process. By understanding the plasma discharge appearing phenomena and properties as plasma temperature, the analysis of near UV and visible spectra collected during the PEO using spatial and time resolved OES provides valuable insights into understanding the processes in the PEO plasma. The arc regime shows atomic or ionic excitation. However, a soft regime does not show atomic or ionic excitation during the PEO process. Also, the soft-regime presents the enhanced ability for a protective oxide coating. The plasma temperature in the arc regime varies in the range of 4200 K to 6400 K, which was calculated using the relative emission intensity of Na-I optical lines. The emission due to collision radiative recombination appears after 130 μs of anodic pulse time in emission spectra during the PEO process. The emission intensity and the plasma temperature show stable behavior until 130 μs of anodic pulse time and 1800 s of the PEO process time and increase with time. Therefore, it can be said that high-intensity plasma discharges, which are responsible for microstructural drawbacks in the formed coating, observed after anodic pulse 130 μs and processing time of 1800 s. It is demonstrated that the growth of the porous layer during the PEO process can be controlled by controlling these timings, which is benefit for the protective oxide coating on a sample. Therefore, the PEO process can be controlled by regulating the anodic to cathodic current ratio, the ON / OFF timing of applied bipolar current pulse, and the PEO process time to improve the performance of the alloy.

References

[1] G.L. Song, A. Atrens, Corrosion Mechanisms of Magnesium Alloys, Advanced Engineering Materials, 1, (1999) 11-33.

[2] W.A. Badawy, N.H. Hilal, M. El-Rabiee, H. Nady, Electrochemical behavior of Mg and some Mg alloys in aqueous solutions of different pH, Electrochimica Acta, 55 (2010) 1880-1887.

[3] A.L. Yerokhin, A. Shatrov, V. Samsonov, P. Shashkov, A. Leyland, A. Matthews, Fatigue properties of Keronite® coatings on a magnesium alloy, Surface and Coatings Technology, 182 (2004) 78-84.

[4] M.K. Kulekci, Magnesium and its alloys applications in automotive industry, The International Journal of Advanced Manufacturing Technology, 39 (2008) 851-865.

[5] D. Zhao, F. Witte, F. Lu, J. Wang, J. Li, L. Qin, Current status on clinical applications of magnesium-based orthopaedic implants: A review from clinical translational perspective, Biomaterials, 112 (2016) 287-302.

[6] K.U. Kainer, F. Kaiser, Magnesium alloys and technology, John Wiley & Sons, 2003.

[7] J. Yang, F.Z. Cui, I.S. Lee, X. Wang, Plasma surface modification of magnesium alloy for biomedical application, Surface and Coatings Technology, 205, Supplement 1 (2010) S182-S187.

[8] B.L. Mordike, T. Ebert, Magnesium: Properties — applications — potential, Materials Science and Engineering: A, 302 (2001) 37-45.

[9] I.J. Polmear, Magnesium Alloys and Applications, Materials Science and Technology, 10 (1994) 1-16.

[10] H. Friedrich, S. Schumann, Research for a "new age of magnesium" in the automotive industry, Journal of Materials Processing Technology, 117 (2001) 276-281.

[11] Y.W. Song, D.Y. Shan, E.H. Han, Electrodeposition of hydroxyapatite coating on AZ91D magnesium alloy for biomaterial application, Materials Letters, 62 (2008) 3276-3279.

[12] J.Y. Chen, X.-B. Chen, J.-L. Li, B. Tang, N. Birbilis, X. Wang, Electrosprayed PLGA smart containers for active anti-corrosion coating on magnesium alloy AMlite, Journal of Materials Chemistry A, 2 (2014) 5738-5743.

[13] H. Duan, K. Du, C. Yan, F. Wang, Electrochemical corrosion behavior of composite coatings of sealed MAO film on magnesium alloy AZ91D, Electrochimica Acta, 51 (2006) 2898-2908.

[14] R. Arrabal, E. Matykina, T. Hashimoto, P. Skeldon, G.E. Thompson, Characterization of AC PEO coatings on magnesium alloys, Surface and Coatings Technology, 203 (2009) 2207-2220.

[15] G. Song, Recent Progress in Corrosion and Protection of Magnesium Alloys, Advanced Engineering Materials, 7 (2005) 563-586.

[16] R.C. Zeng, J. Zhang, W.-j. Huang, W. Dietzel, K.U. Kainer, C. Blawert, W. Ke, Review of studies on corrosion of magnesium alloys, Transactions of Nonferrous Metals Society of China, 16, Supplement 2 (2006) s763-s771.

[17] A.D. King, N. Birbilis, J.R. Scully, Accurate Electrochemical Measurement of Magnesium Corrosion Rates; a Combined Impedance, Mass-Loss and Hydrogen Collection Study, Electrochimica Acta, 121 (2014) 394-406.

[18] F. Lu, A. Ma, J. Jiang, Y. Guo, D. Yang, D. Song, J. Chen, Significantly improved corrosion resistance of heat-treated Mg–Al–Gd alloy containing profuse needle-like precipitates within grains, Corrosion Science, 94 (2015) 171-178.

[19] A. Pardo, M.C. Merino, A.E. Coy, R. Arrabal, F. Viejo, E. Matykina, Corrosion behavior of magnesium/aluminum alloys in 3.5 wt.% NaCl, Corrosion Science, 50 (2008) 823-834.

[20] C. Blawert, W. Dietzel, E. Ghali, G. Song, Anodizing treatments for magnesium alloys and their effect on corrosion resistance in various environments, Advanced Engineering Materials, 8 (2006) 511-533.

[21] H. Huo, Y. Li, F. Wang, Corrosion of AZ91D magnesium alloy with a chemical conversion coating and electroless nickel layer, Corrosion Science, 46 (2004) 1467-1477.

[22] E. Ghali, W. Dietzel, K.-U. Kainer, General and localized corrosion of magnesium alloys: A critical review, Journal of Materials Engineering and Performance, 13 (2004) 7-23.

[23] A.S. Gnedenkov, S.L. Sinebryukhov, D.V. Mashtalyar, S.V. Gnedenkov, Protective properties of inhibitor-containing composite coatings on a Mg alloy, Corrosion Science, 102 (2016) 348-354.

[24] G. Song, A.L. Bowles, D.H. StJohn, Corrosion resistance of aged die cast magnesium alloy AZ91D, Materials Science and Engineering: A, 366 (2004) 74-86.

[25] R.O. Hussein, D.O. Northwood, X. Nie, The influence of pulse timing and current mode on the microstructure and corrosion behavior of a plasma electrolytic oxidation (PEO) coated AM60B magnesium alloy, Journal of Alloys and Compounds, 541 (2012) 41-48.

[26] J.E. Gray, B. Luan, Protective coatings on magnesium and its alloys - a critical review,

Journal of Alloys and Compounds, 336 (2002) 88-113.

[27] G.L. Song, A. Atrens, Understanding magnesium corrosion - A framework for improved alloy performance, Advanced Engineering Materials, 5 (2003) 837-858.

[28] Z. Yao, Z. Jiang, S. Xin, X. Sun, X. Wu, Electrochemical impedance spectroscopy of ceramic coatings on Ti–6Al–4V by micro-plasma oxidation, Electrochimica Acta, 50 (2005) 3273-3279.

[29] S.V. Gnedenkov, O.A. Khrisanfova, A.G. Zavidnaya, S.L. Sinebryukhov, V.S. Egorkin, M.V. Nistratova, A. Yerokhin, A. Matthews, PEO coatings obtained on an Mg–Mn type alloy under unipolar and bipolar modes in silicate-containing electrolytes, Surface and Coatings Technology, 204 (2010) 2316-2322.

[30] J.M. Wheeler, J.A. Curran, S. Shrestha, Microstructure and multi-scale mechanical behavior of hard anodized and plasma electrolytic oxidation (PEO) coatings on aluminum alloy 5052, Surface and Coatings Technology, 207 (2012) 480-488.

[31] M. Curioni, E.V. Koroleva, P. Skeldon, G.E. Thompson, Flow modulated ionic migration during porous oxide growth on aluminum, Electrochimica Acta, 55 (2010) 7044-7049.

[32] A.L. Yerokhin, X. Nie, A. Leyland, A. Matthews, S.J. Dowey, Plasma electrolysis for surface engineering, Surface and Coatings Technology, 122 (1999) 73-93.

[33] H. Li, S. Lu, W. Qin, L. Han, X. Wu, Improving the wear properties of AZ31 magnesium alloy under vacuum low-temperature condition by plasma electrolytic oxidation coating, Acta Astronautica, 116 (2015) 126-131.

[34] X. Nie, A. Leyland, A. Matthews, Deposition of layered bioceramic hydroxyapatite/TiO2 coatings on titanium alloys using a hybrid technique of micro-arc oxidation and electrophoresis, Surface and Coatings Technology, 125 (2000) 407-414.

[35] G.P. Wirtz, S.D. Brown, W.M. Kriven, Ceramic Coatings By Anodic Spark Deposition, Materials and Manufacturing Processes, 6 (1991) 87-115.

[36] M. Mohedano, C. Blawert, M.L. Zheludkevich, Cerium-based sealing of PEO coated AM50 magnesium alloy, Surface and Coatings Technology, 269 (2015) 145-154.

[37] L.O. Snizhko, A.L. Yerokhin, A. Pilkington, N.L. Gurevina, D.O. Misnyankin, A. Leyland, A. Matthews, Anodic processes in plasma electrolytic oxidation of aluminum in alkaline solutions, Electrochimica Acta, 49 (2004) 2085-2095.

[38] L.O. Snizhko, A. Yerokhin, N.L. Gurevina, D.O. Misnyankin, A.V. Ciba, A. Matthews, Voltastatic studies of magnesium anodising in alkaline solutions, Surface and Coatings Technology, 205 (2010) 1527-1531.

[39] E. Cakmak, K.C. Tekin, U. Malayoglu, S. Shrestha, The effect of substrate composition on the electrochemical and mechanical properties of PEO coatings on Mg alloys, Surface and Coatings Technology, 204 (2010) 1305-1313.

[40] J. Liang, P.B. Srinivasan, C. Blawert, W. Dietzel, Influence of pH on the deterioration of plasma electrolytic oxidation coated AM50 magnesium alloy in NaCl solutions, Corrosion Science, 52 (2010) 540-547.

[41] R.O. Hussein, P. Zhang, X. Nie, Y. Xia, D.O. Northwood, The effect of current mode and discharge type on the corrosion resistance of plasma electrolytic oxidation (PEO) coated magnesium alloy AJ62, Surface and Coatings Technology, 206 (2011) 1990-1997.

[42] R. Arrabal, J.M. Mota, A. Criado, A. Pardo, M. Mohedano, E. Matykina, Assessment of duplex coating combining plasma electrolytic oxidation and polymer layer on AZ31 magnesium alloy, Surface and Coatings Technology, 206 (2012) 4692-4703.

[43] Y. Cheng, X. Wu, Z. Xue, E. Matykina, P. Skeldon, G. Thompson, Microstructure, corrosion and wear performance of plasma electrolytic oxidation coatings formed on Ti–6Al–4V alloy in silicate-hexametaphosphate electrolyte, Surface and Coatings Technology, 217 (2013) 129-139.

[44] F. Muhaffel, F. Mert, H. Cimenoglu, D. Höche, M. L. Zheludkevich, C. Blawert, Characterisation and corrosion behavior of plasma electrolytic oxidation coatings on high pressure die cast Mg–5Al–0.4Mn–xCe (x = 0, 0.5, 1) alloys, Surface and Coatings Technology, 269 (2015) 200-211.

[45] A. Yerokhin, L. Snizhko, N. Gurevina, A. Leyland, A. Pilkington, A. Matthews, Special characteristics of discharge phenomena in plasma electrolytic oxidation of aluminum alloy, Surface and Coatings Technology, 177 (2004) 779–783.

[46] C. Wei, X. Tian, S. Yang, X. Wang, R. Fu, P. Chu, Anode current effect in plasma electrolytic oxidation, Surface and Coatings Technology, 201 (2007) 5021–5024.

[47] W. Gu, G. Lv, H. Chen, G. Chen, W. Feng, S. Yang, characterization of ceramic coating produced by plasma electrolytic oxidation of aluminum alloy, Materail science and Engineering:A, 447 (2007) 158–162.

[48] H. Guo, M. An, S. Xu, H. Huo, Formation of oxygen bubbles and its influence on current efficiency in micro-arc oxidation process of AZ91D magnesium alloy, Thin Solid Films 485 (2005) 53–58.

[49] W. Chen, Z. Wang, L. Sun, S. Lu, Research of growth mechanism of ceramic coatings fabricated by micro-arc oxidation on magnesium alloys at high current mode, Journal of Magnesium and Alloys, 3 (2015) 253–257.

[50] A. Yerokhin, A. Shatrov, V. Samsonov, P. Shashkov, A. Pilkington, A. Leyland, A. Matthews, Oxide ceramic coatings on aluminum alloys produced by a pulsed bipolar plasma electrolytic oxidation process, Surface and Coatings Technology, 199 (2005) 150–157.

[51] M. Klapkiv, Simulation of synthesis of oxide-ceramic coatings in discharge channels of a metal-electrolyte system, Materail science, 35 (1999) 279–283.

[52] S. Xin, L. Song, R. Zhao, X. Hu, Influence of cathodic current on composition, structure and properties of Al2O3 coatings on aluminum alloy prepared by micro-arc oxidation process, Thin Solid Films 515 (2006) 326–332.

[53] A. Yabuki, M. Sakai, Anodic films formed on magnesium in organic, silicate-containing electrolytes, Corrossion Science 51 (2009) 793–798.

[54] S. Moon, Y. Jeong, Generation mechanism of microdischarges during plasma electrolytic oxidation of Al in aqueous solutions, Corrossion Science 51 (2009) 1506–1512.

[55] G. Barati, M. Aliofkhazraei, P. Hamghalam, N. Valizade, Plasma electrolytic oxidation of magnesium and its alloys: Mechanism, properties, and applications, Journal of Magnesium and Alloys 5 (2017) 74–132.

[56] Y.G. Ko, E.S. Lee, D.H. Shin, Influence of voltage waveform on anodic film of AZ91 Mg alloy via plasma electrolytic oxidation: Microstructural characteristics and electrochemical responses, Journal of Alloys and Compounds, 586, Supplement 1 (2014) S357-S361.

[57] P.B. Srinivasan, C. Blawert, M. Störmer, W. Dietzel, Characterisation of tribological and corrosion behavior of plasma electrolytic oxidation coated AM50 magnesium alloy, Surface Engineering, 26 (2010) 340-346.

[58] X. Yu, L. Chen, H. Qin, M. Wu, Z. Yan, Formation process of in situ oxide coatings with high porosity using one-step plasma electrolytic oxidation, Applied Surface Science, 366 (2016) 432-438.

[59] Y. Gao, A. Yerokhin, A. Matthews, Deposition and evaluation of duplex hydroxyapatite and plasma electrolytic oxidation coatings on magnesium, Surface and Coatings Technology, 269 (2015) 170-182.

[60] J. Liang, L. Hu, J. Hao, Characterization of microarc oxidation coatings formed on AM60B magnesium alloy in silicate and phosphate electrolytes, Applied Surface Science, 253 (2007) 4490-4496.

[61] L. Chang, Growth regularity of ceramic coating on magnesium alloy by plasma electrolytic oxidation, Journal of Alloys and Compounds, 468 (2009) 462-465.

[62] S. Sarbishei, M.A. Faghihi Sani, M.R. Mohammadi, Effects of alumina nanoparticles

concentration on microstructure and corrosion behavior of coatings formed on titanium substrate via PEO process, Ceramics International, 42 (2016) 8789-8797.

[63] A.L. Yerokhin, X. Nie, A. Leyland, A. Matthews, Characterisation of oxide films produced by plasma electrolytic oxidation of a Ti–6Al–4V alloy, Surface and Coatings Technology, 130 (2000) 195-206.

[64] Y. Gao, A. Yerokhin, A. Matthews, DC plasma electrolytic oxidation of biodegradable cp-Mg: In-vitro corrosion studies, Surface and Coatings Technology, 234 (2013) 132-142.

[65] P.B. Srinivasan, J. Liang, C. Blawert, M. Störmer, W. Dietzel, Effect of current density on the microstructure and corrosion behavior of plasma electrolytic oxidation treated AM50 magnesium alloy, Applied Surface Science, 255 (2009) 4212-4218.

[66] C. Blawert, V. Heitmann, W. Dietzel, H.M. Nykyforchyn, M.D. Klapkiv, Influence of process parameters on the corrosion properties of electrolytic conversion plasma coated magnesium alloys, Surface and Coatings Technology, 200 (2005) 68-72.

[67] J. Liang, L. Hu, J. Hao, Improvement of corrosion properties of microarc oxidation coating on magnesium alloy by optimizing current density parameters, Applied Surface Science, 253 (2007) 6939-6945.

[68] H. Luo, Q. Cai, B. Wei, B. Yu, J. He, D. Li, Study on the microstructure and corrosion resistance of ZrO2-containing ceramic coatings formed on magnesium alloy by plasma electrolytic oxidation, Journal of Alloys and Compounds, 474 (2009) 551-556.

[69] P.B. Srinivasan, J. Liang, R.G. Balajeee, C. Blawert, M. Störmer, W. Dietzel, Effect of pulse frequency on the microstructure, phase composition and corrosion performance of a phosphate-based plasma electrolytic oxidation coated AM50 magnesium alloy, Applied Surface Science, 256 (2010) 3928-3935.

[70] V. Dehnavi, B.L. Luan, X.Y. Liu, D.W. Shoesmith, S. Rohani, Correlation between plasma electrolytic oxidation treatment stages and coating microstructure on aluminum under unipolar pulsed DC mode, Surface and Coatings Technology, 269 (2015) 91-99.

[71] R. Arrabal, E. Matykina, F. Viejo, P. Skeldon, G.E. Thompson, Corrosion resistance of WE43 and AZ91D magnesium alloys with phosphate PEO coatings, Corrosion Science, 50 (2008) 1744-1752.

[72] F. Jaspard-Mécuson, T. Czerwiec, G. Henrion, T. Belmonte, L. Dujardin, A. Viola, J. Beauvir, Tailored aluminum oxide layers by bipolar current adjustment in the Plasma Electrolytic Oxidation (PEO) process, Surface and Coatings Technology, 201 (2007) 8677-8682.

[73] A. Yerokhin, L. Snizhko, N. Gurevina, A. Leyland, A. Pilkington, A. Matthews,

Discharge characterization in plasma electrolytic oxidation of aluminum, Journal of Physics D: Applied Physics, 36 (2003) 2110.

[74] C.S. Dunleavy, I.O. Golosnoy, J.A. Curran, T.W. Clyne, Characterisation of discharge events during plasma electrolytic oxidation, Surface and Coatings Technology, 203 (2009) 3410-3419.

[75] J. Xu, F. Liu, J. Luo, L. Zhao, Effects of Anodic Voltages on Microstructure and Properties of Plasma Electrolytic Oxidation Coatings on Biomedical NiTi Alloy, Journal of Materials Science & Technology, 29 (2013) 22-28.

[76] A.L. Yerokhin, L.O. Snizhko, N.L. Gurevina, A. Leyland, A. Pilkington, A. Matthews, Spatial characteristics of discharge phenomena in plasma electrolytic oxidation of aluminum alloy, Surface and Coatings Technology, 177–178 (2004) 779-783.

[77] S.C. Troughton, A. Nominé, J. Dean, T.W. Clyne, Effect of individual discharge cascades on the microstructure of plasma electrolytic oxidation coatings, Applied Surface Science, 389 (2016) 260-269.

[78] A. Nominé, S.C. Troughton, A.V. Nominé, G. Henrion, T.W. Clyne, High speed video evidence for localised discharge cascades during plasma electrolytic oxidation, Surface and Coatings Technology, 269 (2015) 125-130.

[79] J. Jovović, S. Stojadinović, N.M. Šišović, N. Konjević, Spectroscopic study of plasma during electrolytic oxidation of magnesium- and aluminum-alloy, Journal of Quantitative Spectroscopy and Radiative Transfer, 113 (2012) 1928-1937.

[80] Y. Gao, A. Yerokhin, E. Parfenov, A. Matthews, Application of Voltage Pulse Transient Analysis during Plasma Electrolytic Oxidation for Assessment of Characteristics and Corrosion Behavior of Ca- and P-containing Coatings on Magnesium, Electrochimica Acta, 149 (2014) 218-230.

[81] A. Nominé, J. Martin, G. Henrion, T. Belmonte, Effect of cathodic micro-discharges on oxide growth during plasma electrolytic oxidation (PEO), Surface and Coatings Technology, 269 (2015) 131-137.

[82] Y. Gao, A. Yerokhin, A. Matthews, Effect of current mode on PEO treatment of magnesium in Ca- and P-containing electrolyte and resulting coatings, Applied Surface Science, 316 (2014) 558-567.

[83] F. Jin, P.K. Chu, G. Xu, J. Zhao, D. Tang, H. Tong, Structure and mechanical properties of magnesium alloy treated by micro-arc discharge oxidation using direct current and high-frequency bipolar pulsing modes, Materials Science and Engineering: A, 435 (2006) 123-126.

[84] X.W. Guo, W.J. Ding, C. Lu, C.Q. Zhai, Influence of ultrasonic power on the structure and composition of anodizing coatings formed on Mg alloys, Surface and Coatings Technology, 183 (2004) 359-368.

[85] S. Stojadinovic′, R. Vasilic′, M. Petkovic′, I. Belcǎ, B. Kasalica, M. Peric′, Lj. Zekovic′, Luminescence during anodization of magnesium alloy AZ31, Electrochimica Acta 59 (2012) 354– 359.

[86] Li Wang, Li Chen, Zongcheng Yan, Wen Fu, Optical emission spectroscopy studies of discharge mechanism and plasma characteristics during plasma electrolytic oxidation of magnesium in different electrolytes, Surface & Coatings Technology 205 (2010) 1651–1658.

[87] R.O. Hussein, X. Nie, D.O. Northwood, An investigation of ceramic coating growth mechanisms in plasma electrolytic oxidation (PEO) processing, Electrochimica Acta 112 (2013) 111– 119.

[88] H. Duan, C. Yan, F. Wang, Effect of electrolyte additives on performance of plasma electrolytic oxidation films formed on magnesium alloy AZ91D, Electrochimica Acta, 52 (2007) 3785-3793.

[89] L. Wang, L. Chen, Z. Yan, H. Wang, J. Peng, Effect of potassium fluoride on structure and corrosion resistance of plasma electrolytic oxidation films formed on AZ31 magnesium alloy, Journal of Alloys and Compounds, 480 (2009) 469-474.

[90] Y. Deguchi, Industrial Applications of Laser Diagnostics, CRC Press: Taylor & Francis Group, (2012).

[91] A. Nominé, J. Martin, C. Noël, I.V. Bardin, V.L. Kovalev, T. Belmonte, A.G. Rakoch , G. Henrion, Optical characterization of plasma micro-discharges during Plasma Electroly tic Oxidation on Magnesium, 31st ICPIG Granada Spain, July 14-19, (2013).

[92] M. D. Klapkiv, H.M. Nykyforchyn, and V. M. Posuvailo, Spectral analysis of an elect rolytic plasma in the process of synthesis of aluminum oxide, Material Science 30 (1994) 3 33–343.

[93] S. Stojadinovic, R. Vasilic, M. Petkovic, Z. Nedic, B. Kasalica, I. Belca, Lj. Zekovic, Luminescence properties of oxide films formed by anodization of aluminum in 12-tungsto phosphoric acid, Electrochimica Acta 55 (2010) 3857–3863.

[94] R.O. Hussein, X Nie, D O Northwood, A Yerokhin, A Matthews, Spectroscopic study of electrolytic plasma and discharging behavior during the plasma electrolytic oxidation (PEO) process, Journal of Physics D: Applied Physics 43 (2010) 105203 (13pp).

[95] https://physics.nist.gov/PhysRefData/ASD/lines_form.html

[96] H. Griem, Plasma Spectroscopy, (Cambridge: McGraw-Hill) (1964).

[97] G. Sundararajan, L. Rama Krishna, Mechanisms underlying the formation of thick alumina coatings through the MAO coating technology, Surface and Coatings Technology 167 (2003) 269–277.

[98] F. Tjiang, L.W. Ye, Y.J. Huang, C.C. Chou, D.S. Tsai, Effect of processing parameters on soft regime behavior of plasma electrolytic oxidation of magnesium, Ceramics International 43 (2017) S567–S572.

[99] H.F. Guo, M.Z. An, H.B. Huo, S. Xu, L.J. Wu, Microstructure characteristic of ceramic coatings fabricated on magnesium alloys by micro-arc oxidation in alkaline silicate solutions, Applied Surface Science 252 (2006) 7911-7916.

[100] R. payling, Optical emission lines of atoms and ions, John Wiley & Sons Inc. New York (2000).

[101] X. Yang, Lin Chen, Yao Qu, Run Liu, Kejian Wei, Wenbin Xue, Optical emission spectroscopy of plasma electrolytic oxidation process on 7075 aluminum alloy, Surface & Coatings Technology 324 (2017) 18–25.

[102] S. Ikonopisov, A. Girginov and M. Machrova, Electrical breaking down of barrier anodic films during their formation, Electrochemica Acta, 24(4):45-456, (1979).

[103] N. Klein, Electrical breakdown mechanisms in thin insulators, Thin Solid Films, 50:223-232, (1978).

[104] J.M. Amelia, I. Montero and J. M. Martinez-Duart, A theory of avalanche breakdown during anodic oxidation, Electrochemica Acta 32**:**255-258, (1987).

[105] W. Krysmann, P. Kurze, K-H. Dittrich and H. G. Schnieder, Process characteristics and parameters of Anodic Oxidation by spark discharge (ANOF), Crystal Research and Technology 19:973, (1984).

[106] A. Hickling and M. D. Ingram, Contact glow-discharge electrolysis, Transactions of the Faraday Society 60:783-793 (1964).

[107] R. Liu, Jie Wu, Wenbin Xue, Yao Qu, Chaolin Yang, Bin Wang, Xianying Wu, Discharge behaviors during plasma electrolytic oxidation on aluminum alloy, Material Chemistry and Physics 148 (2014) 284–292.

[108] F. Mécuson, T. Czerwiec, T. Belmonte, L. Dujardin, Diagnostics of an electrolytic microarc process for aluminum alloy oxidation, Surface and Coating Technology 200 (2005) 804–808.

[109] Y. Guan, Y. Xia, G. Li, Growth mechanism and corrosion behavior of ceramic coatings on aluminum produced by auto control AC pulse PEO, Surface Coating Technology 202 (2008) 4602–4612.

[110] C.S. Dunleavy, I. O. Golosnoy, J. A. Curran, T. W. Clyne, Characterization of discharge events during plasma electrolytic oxidation, Surface Coating Technology 203 (2009) 3410-3419.

[111] R.O. Hussein, X. Nie, D. O. Northwood, Influence of process parameters on electrolytic plasma discharging behavior and aluminum oxide coating microstructure, Surface Coating Technology 205 (2010) 1659-1667.